

# Modelling the expected very high energy $\gamma$ -ray emission from accreting neutron stars in X-ray binaries

L. Ducci,<sup>1,2,3\*</sup> P. Romano,<sup>3</sup> S. Vercellone,<sup>3</sup> A. Santangelo<sup>1</sup>

<sup>1</sup>*Institut für Astronomie und Astrophysik, Kepler Center for Astro and Particle Physics, University of Tübingen, Sand 1, 72076 Tübingen, Germany*

<sup>2</sup>*ISDC Data Center for Astrophysics, Université de Genève, 16 chemin d'Écogia, 1290 Versoix, Switzerland*

<sup>3</sup>*INAF – Osservatorio Astronomico di Brera, Via E. Bianchi 46, I-23807, Merate, Italy*

Accepted XXX. Received YYY; in original form ZZZ

## ABSTRACT

The detection of  $\gamma$ -ray emission from accreting pulsars in X-ray binaries (XRBs) has long been sought after. For some high-mass X-ray binaries (HMXBs), marginal detections have recently been reported. Regardless of whether these will be confirmed or not, future telescopes operating in the  $\gamma$ -ray band could offer the sensitivity needed to achieve solid detections and possibly spectra. In view of future observational advances, we explored the expected emission above 10 GeV from XRBs, based on the Cheng & Ruderman model, where  $\gamma$ -ray photons are produced by the decay of  $\pi^0$  originated by protons accelerated in the magnetosphere of an accreting pulsar fed by an accretion disc. We improved this model by considering, through Monte Carlo simulations, the development of cascades inside of and outside the accretion disc, taking into account pair and photon production processes that involve interaction with nuclei, X-ray photons from the accretion disc, and the magnetic field. We produced grids of solutions for different input parameter values of the X-ray luminosity ( $L_x$ ), magnetic field strength ( $B$ ), and for different properties of the region where acceleration occurs. We found that the  $\gamma$ -ray luminosity spans more than five orders of magnitude, with a maximum of  $\sim 10^{35}$  erg s<sup>-1</sup>. The  $\gamma$ -ray spectra show a large variety of shapes: some have most of the emission below  $\sim 100$  GeV, others are harder (emission up to 10–100 TeV). We compared our results with *Fermi*/LAT and VERITAS detections and upper-limits of two HMXBs: A0535+26 and GRO J1008–57. More consequential comparisons will be possible when more sensitive instruments will be operational in the coming years.

**Key words:** accretion, accretion discs - X-ray:binaries - gamma-rays:stars - stars:neutron - individual: A0535+26, GRO J17008–57

## 1 INTRODUCTION

X-ray binaries (XRBs) are systems usually composed by a compact object (neutron star, black hole, white dwarf) and a normal star (often called “donor star”). The X-ray emission is produced by the conversion of the gravitational potential energy of the accreted matter into radiation (see, e.g., Shklovsky 1967). XRBs are usually divided in two main classes: high-mass X-ray binaries (HMXBs) and low-mass X-ray binaries (LMXBs). In HMXBs, the donor star is massive ( $\gtrsim 8 M_\odot$ ) and of OB spectral type. The compact object accretes the dense stellar wind ejected by the companion star, and the accretion can be either spherically symmetric or mediated by an accretion disc. In LMXBs, the donor star is less massive than the Sun and usually it transfers mass by Roche Lobe overflow. Usually, an accretion disc forms around the compact object (see, e.g., Davidson & Ostriker 1973; Treves et al. 1988; van Paradijs 1998). For both classes, X-ray emission can be either persistent or transient. X-ray luminosity ranges from  $\sim 10^{31}$  erg s<sup>-1</sup> to  $\sim 10^{39}$  erg s<sup>-1</sup>, and the bulk of the emission is in the band  $\sim 0.1 - 100$  keV (see, e.g., Revnivtsev & Mereghetti 2015). Within this energy range, spectra can be softer or harder, depending on many physical conditions (e.g. Makishima et al. 1986; White et al. 1995). The orbital periods range from few hours (for example, the ultra-compact binaries, Di Salvo & Sanna 2022) to few years (e.g. Bhadkamkar & Ghosh 2012).

Since the birth of  $\gamma$ -ray astronomy, XRBs received special attention, because they were considered candidates for the origin of a substantial fraction of the Galactic cosmic rays. In particular, it has been proposed that particles accelerated in XRBs might contribute to the Galactic cosmic-ray sea (Heinz & Sunyaev 2002). Part of the interest on XRBs was fueled further by the alleged  $\sim 40$  detections obtained between 1975 and 1990 at energies  $\sim 35$  MeV–5 GeV (SAS-2) and around 1 TeV in the directions of Her X–1, Vela X–1, Cen X–3, 4U 1145–619, 4U 0115+63, 4U 1626–67, Sco X–1, Cyg X–3, SMC X–1, LMC X–4, and X0021.8–7221 (Weekes 1988; Bonnet-Bidaud & Chardin 1988; Chadwick et al. 1990; Ong 1998, and references therein). Many of these detections were marginally significant and were not confirmed in the subsequent years by more sensitive experiments, casting doubts on their truthfulness (Ong 1998; Dubus 2013).

In the late 1970s, the discovery of X-ray emission from the Be/X-ray binary (Be/XRB) LS I+61°303 was also important (although it played

\* E-mail: ducci@astro.uni-tuebingen.de (LD)

**Table 1.** List of XRBs with a  $\gamma$ -ray counterpart candidate of interest for this work.

Name	Type <sup>a</sup>	$P_{\text{spin}}$ (s)	B (G)	Name $\gamma$ -ray counterpart	Type of association <sup>b</sup>	References
A0535+26	Be/XRB	103.4	$4 \times 10^{12}$	3EG J0542+2610	p,t,o	1, 2, 3, 4
GRO J1008–57	Be/XRB	93.6	$7 - 8 \times 10^{12}$	-	p,t,o	5, 3
4U 1036–56	Be/XRB	853	-	AGL J1037–5708; GRO J1036–55	p	6
IGR J17354–3255	SFXT	-	-	AGL J1734–3310	p	7, 8
IGR J11215–5952	SFXT	186	-	3EG J1122–5946	p	9, 8
AX J1841.0–0536	SFXT	-	-	3EG J1837–0423, HESS J1841–055	p	10, 8
SAX J1324.4–6200	Be/XRB	172.8	-	-	p	3
1H 0749–600	Be/XRB	-	-	-	p	3
1H 1238–599	HMXB	3.2 or 4.3	-	-	p	3
IGR J17544–2619	SFXT	-	$1.5 \times 10^{12}$	-	p	3
RX J2030.5+4751	Be/XRB	-	-	-	p	3

<sup>a</sup> Sub-classes of XRBs. Be/XRB indicates the subclass of HMXBs with a Be type donor star (see, e.g., [Reig 2011](#)). SFXT is for: supergiant fast X-ray transient, a subclass of HMXBs (see, e.g., [Romano 2015](#); [Sidoli 2013](#)); <sup>b</sup> positional: *p*; time variability correlation: *t*; orbital variability correlation: *o*. References: (1) [Romero et al. \(2001\)](#); (2) [Torres et al. \(2001\)](#); (3) [Harvey et al. \(2022b\)](#); (4) [Hou et al. \(2023\)](#); (5) [Xing & Wang \(2019\)](#); (6) [Li et al. \(2012\)](#); (7) [Sguera et al. \(2011\)](#); (8) [García et al. \(2014\)](#); (9) [Sguera \(2009\)](#); (10) [Sguera et al. \(2009\)](#).

a much more fundamental role in the birth of the class of “gamma-ray binaries”, that finally emerged in 2000s; (see, e.g., [Dubus 2013](#), and references therein).  $\gamma$ -ray binaries host a compact object (pulsar or black-hole) and a massive OB type star. In gamma-ray binaries, the bulk of the emission is in the  $\gamma$ -ray band. They also show characteristic variability in the radio band. The main physical processes proposed for their  $\gamma$ -ray emission are particles accelerated in relativistic jets (microquasar scenario) or interaction between the winds of a pulsar and the companion star ([Dubus 2006](#); [Mirabel 2006](#); [Romero et al. 2007](#); [Paredes & Bordas 2019](#)). Their relatively weak X-ray emission and their overall multiwavelength properties suggest they form a distinct class from the typical XRBs, for which most of the emission in the X-ray band is due to accretion. Therefore,  $\gamma$ -ray binaries are not the subject of this paper.

Following the controversial XRB findings mentioned above, thanks to the advent of new instruments such as the Energetic Gamma Ray Experiment Telescope (EGRET, 30 MeV–10 GeV) on board of the Compton Gamma Ray Observatory (CGRO) satellite ([Kanbach et al. 1989](#)), the Large Area Telescope (LAT) on board of the *Fermi* satellite ( $\sim 20$  MeV–300 GeV; [Atwood et al. 2009](#)), and the Astrorivelatore Gamma a Immagini LEggero *AGILE* (30 MeV–50 GeV; [Tavani et al. 2009](#)), recently there have been other detections of XRBs (which do not fall into the category of  $\gamma$ -ray binaries). For some of them the association between the X-ray and the  $\gamma$ -ray sources is circumstantial, being based only on positional coincidence. For others, a detection (often only marginal) of the  $\gamma$ -ray source is reported at some orbital phases or specific time intervals which correspond to epochs in which the X-ray counterpart is in a particular luminosity state (e.g. during X-ray outbursts, or in their temporal proximity). Table 1 shows a list of the sources recently detected, which are of interest for our work. From the list of sources reported in [Harvey et al. \(2022b\)](#) we did not consider the “false positive” sources and those which have an unlikely association with the X-ray counterpart.

All the  $\gamma$ -ray detections with potential XRBs as counterparts collected since 1975 stimulated the development of numerous hypotheses and models to explain the  $\gamma$ -ray emission produced in accreting XRBs. In order to offer a compact review of all the models that, to our knowledge, have been presented so far, and to put our calculations (Sect. 2) in the broader context of all the models proposed, we summarised them below. Since our calculations are based on [Cheng & Ruderman \(1989\)](#) (hereafter: [CR89](#)) model, this is described more extensively in Sect. 1.1, while the other models are reported in Sect. 1.2.

### 1.1 Accelerating gaps in magnetospheres of pulsars with accretion discs and production of $\gamma$ -ray emission

To account for the numerous detections of  $\gamma$ -ray emission from accreting X-ray pulsars, [CR89](#) proposed a mechanism to accelerate particles in the magnetosphere of a pulsar surrounded by an accretion disc. This mechanism was able to achieve photon energies up to  $\sim 100$  TeV. The rotational and magnetic dipole field axes were assumed to be aligned, and the accretion disc to lie on the equatorial plane of the pulsar. [CR89](#) showed that when the inner part of the accretion disc rotates faster than the pulsar, a part of the magnetosphere corotates with the pulsar and another part with the sector of the accretion disc to which it is linked by the magnetic field. These two regions which rotate with different velocities are separated by gaps which are in principle empty of plasma. A potential drop forms in the gaps and it can reach  $\sim 10^{15} - 10^{16}$  V. The gap potential drop can accelerate protons toward the accretion disc, which becomes a target for  $\pi^0$  production and consequently high-energy photons. [Cheng et al. \(1991\)](#) showed that the  $\gamma$ -ray photons produced by the  $\pi^0$  decay, called “primary”, can be converted to  $e^\pm$  pairs by the magnetic field, which in turn, produce synchrotron secondary  $\gamma$ -ray photons. Assuming the typical parameters for accreting X-ray pulsars, they found that the total  $\gamma$ -ray power emitted was just two orders of magnitude lower than the total X-ray power from accretion. Their results were in good agreement with the alleged detections obtained in the years 1975–1990 (see Sect. 1). [CR89](#) explained also the short bursts ( $\sim 10^3$  s) of  $\gamma$ -ray emission which were claimed to have been observed in some XRBs. It was proposed that they were the result of  $\gamma$ -ray

photons able to escape from radially moving annuli in the accretion disc having relatively low local density. Elsewhere, the accretion disc was sufficiently thick to absorb all the  $\gamma$ -ray photons produced in the disc. Cheng & Ruderman (1991) extended the study of the properties of the magnetosphere and the accelerating gap to the cases in which the inner part of the accretion disc has the same or lower rotational velocity of the pulsar. The model by CR89 was based on the approximation that X-ray photons produced by the accretion at the stellar surface (including the accretion column) are strongly shielded by the accreting matter. This approximation was supported by the sufficiently high grammage of the material channeled along the magnetic field lines by the gravitational field, from the inner regions of the accretion disc to the stellar surface. However, as pointed out by Cheng & Ruderman (1991) and Cheng et al. (1992), the shielding effect may not be efficient enough. In this case (called “weak shielding” or “pair production limited”), some of the X-ray photons from the stellar surface are boosted up to  $\gamma$ -rays by inverse Compton scattering with the  $e^\pm$  accelerated in the gap. These  $\gamma$ -rays then transform to  $e^\pm$  pairs by collisions with other X-ray photons. The newly created electrons and positrons are then accelerated by the gap and then boost up other X-ray photons to higher energies. This mechanism leads to an overall reduction of the potential drop across the gap, whose formulation was presented in Cheng & Ruderman (1991) and Cheng et al. (1992).

The acceleration mechanism originally proposed by CR89 included only the hadronic part, that is the acceleration of protons. Cheng et al. (1992) showed that the proton current directed toward the disc must be balanced by an opposite flow of electrons that cancels any net charge density from the current flow, and keep steady the potential drop across the gap. These electrons lose their energies through the development of cascades based on synchrotron, curvature, and photon-photon interactions. The mechanism continues until the energies of the  $\gamma$ -ray photons allow the production of pairs of  $e^\pm$ . Cheng et al. (1992) considered the “leptonic branch” in the framework of strongly shielded gap. In their calculations, the expected  $\gamma$ -ray emission is steady and softer ( $\lesssim 10^{7-8}$  eV) compared to that produced by the hadronic branch of the CR89 model.

Bednarek (1993, 1997, 2000) and Sierpowska & Bednarek (2005) discussed the role played by the anisotropic thermal radiation fields emitted by the accretion disc around the pulsar and by the companion star. They assumed that the spectra of the primary  $\gamma$ -ray photons or leptons (of unknown origin) were injected in the binary system, from the compact object, and were propagating in an anisotropic radiation field. Their calculations considered different angles of observations. They demonstrated that the observed  $\gamma$ -ray emission can show an orbital modulation, and in some cases it can be quenched by the radiation field emitted by the accretion disc.

In a series of papers, Romero et al. (2001); Orellana & Romero (2005), and Orellana et al. (2007), improved the hadronic model first proposed by CR89, always retaining the hypothesis of a strongly shielded gap. Then, they applied it to the case of the Be/XRB A0535+26. The main innovations introduced were the production of electromagnetic cascades within the accretion disc under the “approximation A” (calculations described in Rossi & Greisen (1941), in which bremsstrahlung and pair production from the interactions of photons with atoms/nuclei are considered, while ionization losses, Compton collisions are neglected and the cross section for bremsstrahlung and pair production are considered in their relativistic limits). For the production of cascades outside the accretion disc, they considered pair production in photon-photon collisions and Inverse Compton scattering. They presented the expected general properties of the  $\gamma$ -ray spectrum for A0535+26 for some specific cases. They assumed a pitch angle for the particles and photons involved in the cascades of  $45^\circ$  with respect to a normal line to the accretion disc plane, to take into account the angle of misalignment between the spin and magnetic axes, and a beaming factor of 0.3.

Zhang et al. (2014a) performed numerical calculations of the cascade processes in accreting XRBs in the framework of the leptonic scenario proposed by Cheng et al. (1992) and, as an example, compared their results with the observations of the  $\gamma$ -ray binary LS I +61° 303.

In our work, we consider the hadronic model by CR89 in the cases of strongly and weakly shielded gaps, considering more types of interaction processes for the production of cascades. In our calculations, we also take into account the role played by the poloidal magnetic field inside the accretion disc. Some of the details about the CR89 model on which our calculations are strongly linked are thus described separately from this introductory section, and can be found in Sect. 2.

## 1.2 Other models for the $\gamma$ -ray emission from XRBs

In addition to the CR89 model and its sub-variants, other ideas and models have been presented so far for the  $\gamma$ -ray emission from XRBs. Below, we briefly describe them, and in Fig. 1 we show a schematic overview of all these models, including CR89.

Katz & Smith (1988) and Smith et al. (1992) argued that protons trapped in the closed magnetosphere of a NS or a white dwarf, bouncing along the dipole magnetic field lines between the poles, can be accelerated to  $10^{16-17}$  eV by plasma turbulences. The trapped protons gradually accelerate to high energies, until they escape the closed magnetosphere. Significant  $\gamma$ -ray emission occurs if the protons hit dense regions of matter, such as an accretion disc, the accretion column, or the surface of the companion star. This mechanism can in principle explain  $\gamma$ -ray emission up to  $\sim 10^{15}$  eV. Walter (2007) showed that if the targets of protons are sufficiently dense clumps of stellar winds expelled by an OB supergiant star companion and accreted by the compact object, supergiant HMXBs could be transient TeV sources (see, however, also Sguera et al. 2009).

Rudak & Meszaros (1991) calculated the photon spectrum produced by the injection of a power law proton energy distribution in the magnetosphere of an accreting NS. The photon spectrum is produced by the interaction of protons with the accreting NS X-ray radiation field and the magnetospheric field. The results presented in Rudak & Meszaros (1991) are dependent on the input proton spectrum, and therefore on the mechanism that accelerates them. As an example, they carried out the calculations in the framework of the Kiraly & Meszaros (1988) corotating jet model, and found that if the input proton energy distribution is a power law with slope  $\Gamma_p = 2$  and extends up to  $E_p \approx 10^{16}$  eV, the secondary photon spectrum extends from MeV to the PeV range.

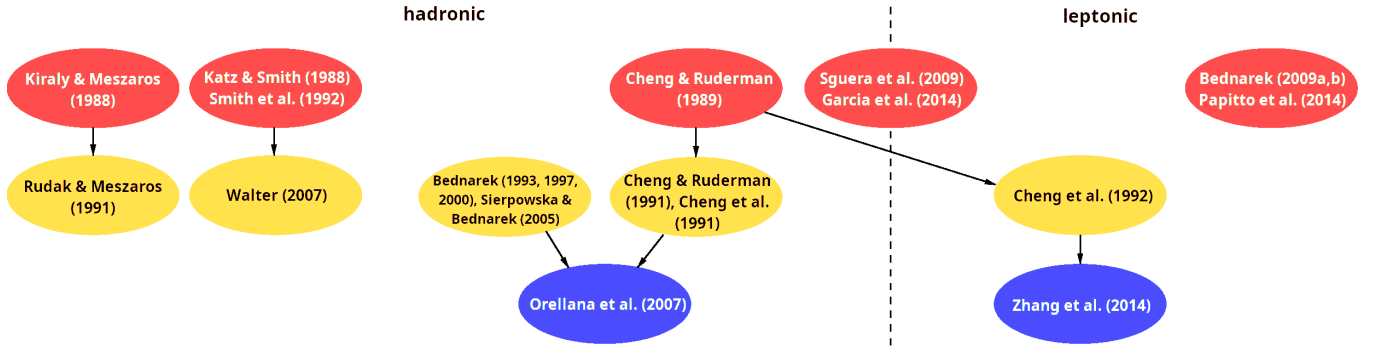


**Figure 1.** Schematic illustration of all the models proposed for the  $\gamma$ -ray emission from accreting X-ray binaries (to the best of our knowledge). They are divided into hadronic and leptonic models. Models in red ellipses include the mechanism of production of particle acceleration and production of primary  $\gamma$ -ray photons. Models in yellow ellipses assume a mechanism of acceleration of particles and production of primary photons. If they are strictly based on one of them, they are connected with an arrow. Models in blue ellipses are further development of previous models.

The model described in [Bednarek \(2009a,b\)](#) shows that at the Alfvén radius a turbulent and magnetized transition region forms, which provides favorable conditions for the acceleration of electrons to relativistic energies. If a fraction of matter falls onto the neutron star (NS) surface, it produces thermal radiation which interacts with the accelerated electrons. If accretion is prevented by a gating mechanism, the relativistic electrons can still interact with the radiation field of the companion star. Electrons will lose energy through synchrotron and Inverse Compton processes and can produce  $\gamma$ -ray emission up to the GeV energy range. This mechanism has been used to discuss the  $\gamma$ -ray emission from the Be/XRB 4U 1036–56, which has an *AGILE* and a *CGRO* counterpart, AGL J1037–5708 and GRO J1036–55 ([Li et al. 2012](#)). A similar model was proposed by [Papitto et al. \(2014\)](#) to explain the  $\gamma$ -ray emission of the LMXB XSS J12270-4859.

Positional associations between some supergiant fast X-ray transients (SFXTs)<sup>1</sup> with unidentified  $\gamma$ -ray transient sources detected by *AGILE* and *EGRET* ([Sguera et al. 2009](#); [Sguera 2009](#); [Sguera et al. 2011](#)) have been reported. [García et al. \(2014\)](#) showed that the magnetic field strength in NSs accreting from the stellar wind of a companion OB supergiant star can decay to sufficiently low values ( $B \approx 10^8$  G) to enable the formation of relativistic jets. For one of them, AX J1841.0–0536, it was proposed that it hosts a low magnetized pulsar where  $\gamma$ -ray emission is due to transient jets produced by the sporadic accretion of clumps from the supergiant companion star ([Sguera et al. 2009](#)).

## 2 CALCULATIONS

### 2.1 Mechanism of acceleration of the protons

In the [CR89](#) model, a magnetized NS fed by an accretion disc is considered. They show that a conelike gap around the null-surface  $\vec{\Omega}_* \cdot \vec{B} = 0$  forms when the angular velocity of the disc  $\Omega_d$  at the inner radius of the disc ( $R_0$ ) exceeds the angular velocity of the star ( $\Omega_*(R_0) < \Omega_d(R_0)$ ). This gap separates regions with opposite charges, and a strong potential drop develops within it ([Fig. 2](#)).

If the gap is efficiently shielded by the accretion flow channeled by the magnetic field lines from  $\sim R_0$  to the NS surface, it can be considered, in first approximation, empty of plasma. In this case, called “strong shielding”, [CR89](#) showed that the potential drop across the gap approaches the value:

$$\Delta V_{\text{strong}} \approx 4 \times 10^{14} \beta^{-5/2} \left( \frac{M}{M_\odot} \right)^{1/7} R_6^{-4/7} L_{x,37}^{5/7} B_{12}^{-3/7} \text{ V}, \quad (1)$$

where  $M$  is the mass of the NS,  $R_6$  (in units of  $10^6$  cm) is its radius,  $B_{12}$  (in units of  $10^{12}$  G) is the magnetic field,  $L_{x,37}$  (in units of  $10^{37}$  erg s<sup>-1</sup>) is the X-ray luminosity produced by the accretion,  $\beta = 2R_0/R_A$ , where:

$$R_0 = 1.35 \gamma_0^{2/7} \eta^{4/7} R_A \quad (2)$$

$$R_A = \mu^{4/7} \dot{M}^{-2/7} (2GM)^{-1/7}, \quad (3)$$

where  $R_0$  is defined according to the work by [Wang \(1996\)](#),  $R_A$  is the Alfvén radius,  $\gamma_0 = -B_{\theta_0}/B_{z_0} \approx 1$  is the magnetic pitch angle,  $\eta$  is the screening factor (it is assumed a partially screened disc  $\eta = 0.1$ )<sup>2</sup>,  $\mu = BR_{\text{NS}}^3/2$  is the dipolar magnetic moment, and  $\dot{M}$  is the mass accretion rate.

If the gap is weakly shielded, the potential drop across the gap is:

$$\Delta V_{\text{weak}} \approx 6 \times 10^{11} L_{x,37} \left( \frac{E_x}{1 \text{ keV}} \right)^{-1} R_6^{-1} B_{12}^{-1/2} \text{ V}, \quad (4)$$

<sup>1</sup> SFXTs are a sub-class of HMXBs where the donor star is OB type supergiant, and the compact object shows a peculiar fast X-ray variability, with a dynamic range up to  $10^{5-6}$  on timescales of  $\sim 10^4$  s (see, e.g., [Romano 2015](#); [Sidoli 2013](#)).

<sup>2</sup>  $\eta$  takes into account the screening effects of the currents induced in the surface of the accretion disc.

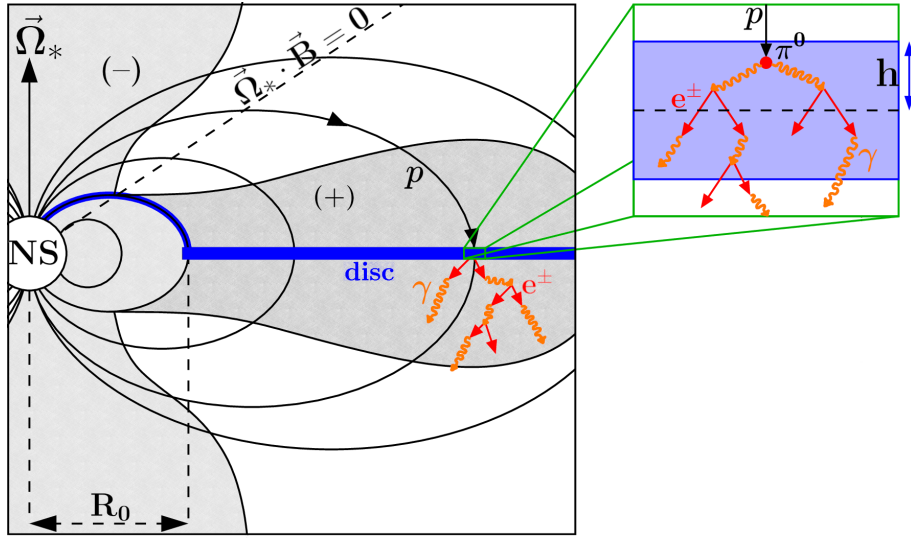


**Figure 2.** Schematic illustration of the Cheng & Ruderman magnetosphere model (not in scale) when  $\Omega_*(R_0) < \Omega_d(R_0)$ . The light gray regions corotate with the NS, while the dark gray regions corotate with the accretion disc. A cone-like gap around the null surface  $\vec{\Omega}_* \cdot \vec{B} = 0$  forms, where protons from the NS are accelerated toward the accretion disc. Their interaction with it produce  $\gamma$ -ray primary photons via  $\pi^0$  decay. In turn, primary photons develop cascades of  $e^\pm$  pairs (red arrows) and other  $\gamma$ -ray photons (orange wavy arrows) inside the accretion disc and in the opposite side of it.

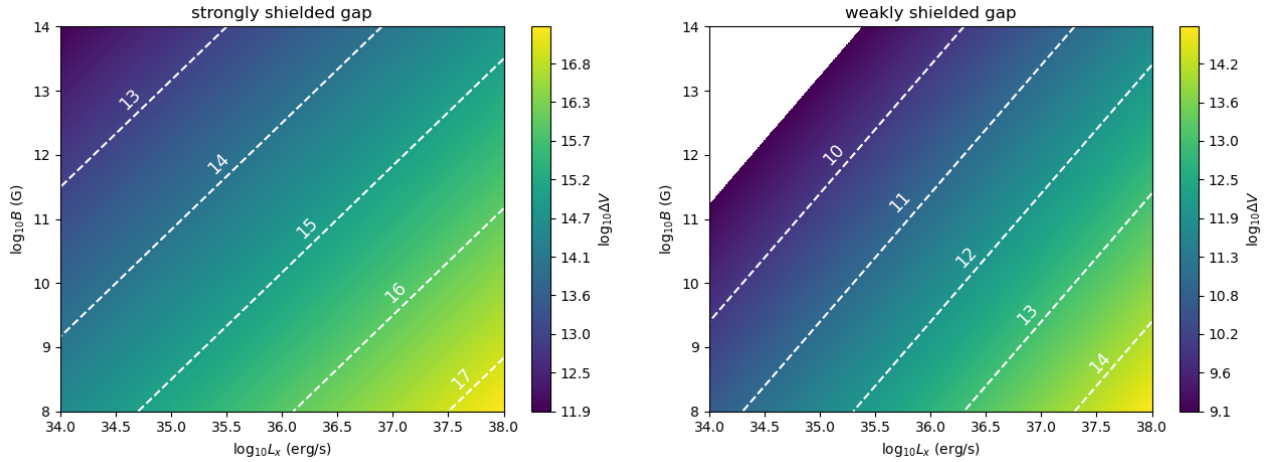


**Figure 3.** Comparison of the potential drops in the gaps for strongly (left) and weakly shielding (right) cases, as function of the X-ray luminosity and magnetic field strength (at the surface of the NS). The white region in the right panel corresponds to  $E_p < E_{th}$ , where the approximations used in this work are not valid. Dashed white lines show contours which have the same units used for the respective colour bars.

where  $E_x$  is the characteristic energy of the X-ray photons (Cheng & Ruderman 1991; Cheng et al. 1992).

Figure 3 shows  $\Delta V_{strong}$  and  $\Delta V_{weak}$  for different values of  $L_{x,37}$  and  $B_{12}$  (Equations 1 and 4). We assumed  $M/M_\odot = 1.4$  and  $R_6 = 1.2$ .

The maximum current of protons that can flow through the gap is (CR89):

$$J_{max} \approx 1.5 \times 10^{24} \beta^{-2} \left( \frac{M}{M_\odot} \right)^{-2/7} R_6^{1/7} L_{x,37}^{4/7} B_{12}^{-1/7} \text{esu s}^{-1}. \quad (5)$$

Figure 4 shows  $J_{max}/e$  (based on Eq. 5, for different values of  $L_{x,37}$  and  $B_{12}$ ).

## 2.2 Production of the primary $\gamma$ -ray photons

Relativistic protons accelerated in the gap can produce  $\pi^0$ -mesons through inelastic collisions with protons of the accretion disc. The decays of  $\pi^0$  then produce  $\gamma$ -rays which we call primary photons. We follow the formalism presented by Aharonian & Atayan (1996, 2000) and adopted by Orellana et al. (2007) to calculate the emissivity of  $\gamma$ -rays in this case.

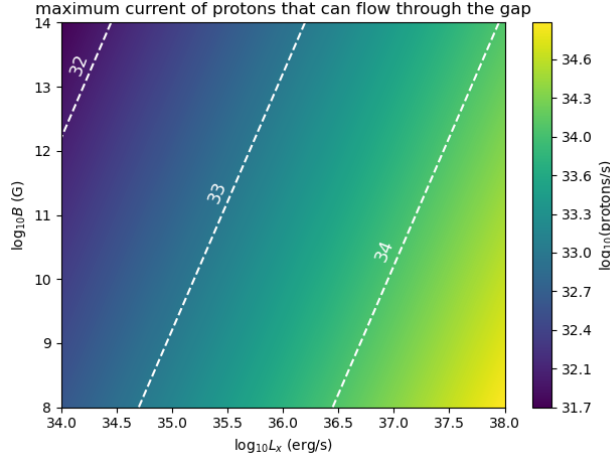


**Figure 4.** Maximum current of protons that can flow through the gap, as function of the X-ray luminosity and magnetic field strength (at the surface of the NS). Dashed white lines show contours which have the same units used for the colour bar.

The pion emissivity  $q_{\pi^0}(E_{\pi^0})$  can be calculated in the  $\delta$ -function approximation:

$$q_{\pi^0}(E_{\pi^0}) = n_p \int_{E_{\text{th}}}^{\infty} \delta(E_{\pi^0} - \kappa E_{\text{kin}}) J_p(E_p) \sigma_{pp} dE_p = \frac{n_p}{\kappa} \sigma_{pp} \left( m_p c^2 + \frac{E_{\pi^0}}{\kappa} \right) J_p \left( m_p c^2 + \frac{E_{\pi^0}}{\kappa} \right), \quad (6)$$

where  $n_p$  is the density of proton targets,  $E_{\text{th}}$  is the proton energy threshold for the production of  $\pi^0$ ,  $\kappa$  ( $\sim 0.17$  in the broad energy range GeV to TeV) is the mean fraction of kinetic energy of the proton ( $E_{\text{kin}} = E_p - m_p c^2$ ) transferred to the secondary  $\pi^0$  in a collision (it includes about 6% of contribution from the  $\eta$ -meson production, [Gaisser 1990](#)),  $J_p(E_p)$  is the proton injected spectrum,  $\sigma_{pp}$  is the total cross-section of inelastic  $pp$  collisions, well approximated above  $\sim 10$  GeV by:

$$\sigma_{pp} \approx 30[0.95 + 0.06 \ln(E_{\text{kin}}/\text{GeV})] \times 10^{-27} \text{ cm}^2 \quad (7)$$

([Aharonian & Atoyan 1996](#)). For  $J_p$ , we follow the approximation proposed by [Orellana et al. \(2007\)](#) that protons reach the accretion disc with the same energy gained in the gap:  $E_p \approx e\Delta V_{\text{max}}$ . The proton injected spectrum is thus mono-energetic:

$$J_p(E) = \frac{J_{\text{max}}}{e\Sigma} \delta(E - E_p) \frac{\text{protons}}{\text{s cm}^2}, \quad (8)$$

where  $\Sigma$  is the area of the accretion disc crossed by the protons.

The  $\gamma$ -ray emissivity due to  $\pi^0$  decay is:

$$q_{\gamma}(E_{\gamma}) = 2 \int_{E_{\pi^0}^{\text{min}}(E_{\gamma})}^{\infty} \frac{q_{\pi^0}(E_{\pi^0})}{\sqrt{E_{\pi^0}^2 - m_{\pi^0}^2 c^4}} dE_{\pi^0}, \quad (9)$$

where  $E_{\pi^0}^{\text{min}}(E_{\gamma}) = E_{\gamma} + (m_{\pi^0}^2 c^4)/(4E_{\gamma})$ ,  $m_{\pi^0}$  is the  $\pi^0$  rest mass (e.g., [Cavallo & Gould 1971](#)).

From Equations. 9, 6, and 8, the rate of production of primary photons inside the disc is:

$$\frac{dN_{\gamma}}{dt dE_{\gamma}} \approx \frac{2J_{\text{max}} n_p}{e} \frac{\sigma_{pp}(E_p)}{\sqrt{\kappa^2 (E_p - m_p c^2)^2 - m_{\pi^0}^2 c^4}} \int_0^{2h} e^{-z/\lambda_{pp}} dz \frac{\text{photons}}{\text{s eV}}, \quad (10)$$

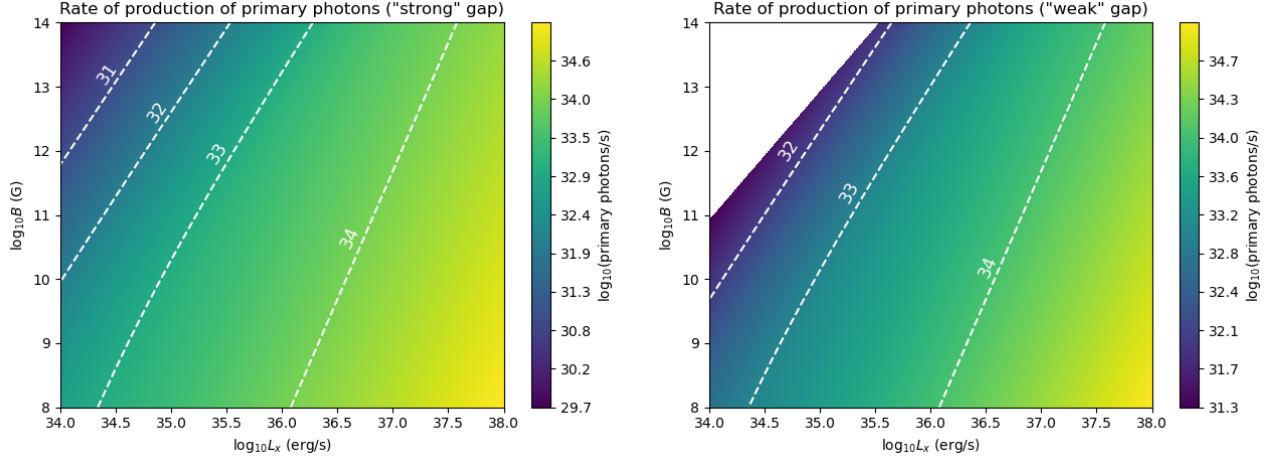
where  $E_{\gamma}$  ranges between  $E_{\text{inf}} = 0.5E_{\pi^0}(1 - v_{\pi^0}/c)$  and  $E_{\text{sup}} = 0.5E_{\pi^0}(1 + v_{\pi^0}/c)$  ( $dN_{\gamma}/dt dE_{\gamma} = 0$  outside of this range),  $v_{\pi^0}$  is the velocity of the pion with energy  $E_{\pi^0} = \kappa(E_p - m_p c^2)$  (e.g., [Stecker 1971](#)),  $h$  is half thickness of the accretion disc, and  $\lambda_{pp} = 1/(\sigma_{pp} n_p)$  is the mean free path of the proton entering into the disc.

Figure 5 shows the rate of production of primary photons (Eq. 10 integrated over the energy) assuming gaps for strongly and weakly shielding cases, for different values of  $L_{x,37}$  and  $B_{12}$ . Similarly, Fig. 6 shows the maximum energy achieved by the primary photons.

### 2.3 Accretion disc structure and configuration of the magnetic field

To parametrize the thickness  $h$ , density  $n_p$ , and temperature  $T$  of the disc as a function of radius and mass accretion rate, we adopted the analytic solution for the standard accretion disc structure presented in [Vietri \(2008\)](#), which is a slightly modified version of that presented first by [Shakura & Sunyaev \(1973\)](#) and later by [Treves et al. \(1988\)](#), in a version better suited to astrophysical applications.

We assume a dipole magnetic field aligned with the rotational axis of the NS. To describe the main properties of the NS magnetic field inside the accretion disc, we consider the magnetically threaded disc (MTD) model. Many versions of this model have been proposed (see, e.g., [Ghosh & Lamb 1979a,b](#); [Wang 1995](#) and, for a review, [Ghosh 2007](#)) and numerous analytical and numerical studies have been carried out



**Figure 5.** Rate of production of primary photons assuming gaps for strongly (left) and weakly shielding (right) cases, as function of the X-ray luminosity and magnetic field strength (at the surface of the NS). The white region in the right panel corresponds to  $E_p < E_{th}$ , where the approximations used in this work are not valid. Dashed white lines show contours which have the same units used for the respective colour bars.

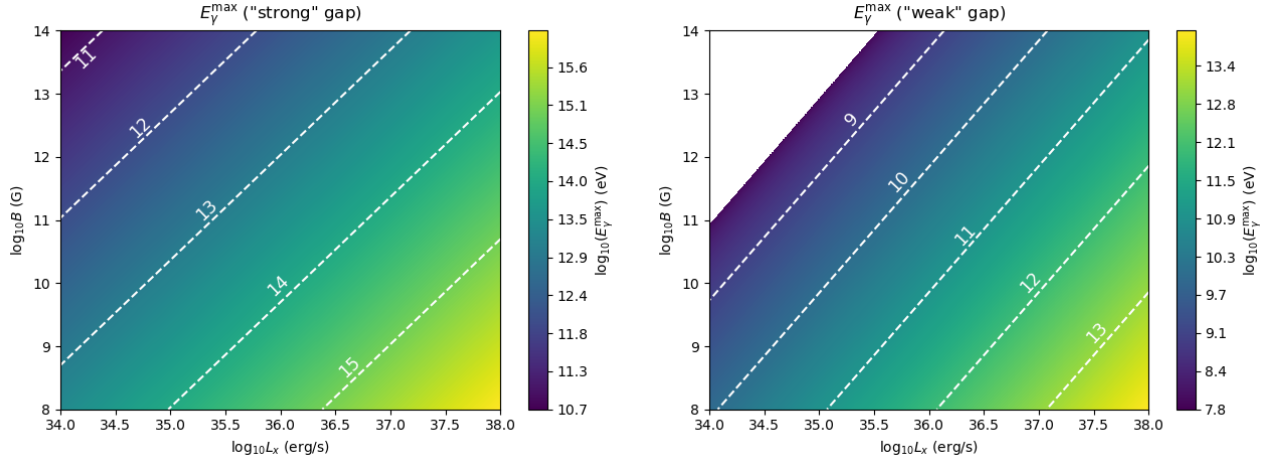


**Figure 6.** Maximum energy  $E_{\gamma}^{\max}$  achieved by the primary photons assuming gaps for strongly (left) and weakly shielding (right) cases, as function of the X-ray luminosity and magnetic field strength (at the surface of the NS). The white regions in the right panels have  $E_p < E_{th}$ , where the approximations used in this work are not valid. Dashed white lines show contours which have the same units used for the respective colour bars.

(e.g. Campbell 1987, Kluźniak & Rappaport 2007, Naso et al. 2013, Jafari & Vishniac 2018, Romanova et al. 2021, and references therein). The idea behind this model is that the magnetic field lines crossing the disc are distorted in the  $\phi$ -direction to form a poloidal field component, due to the shearing motion between the differential rotation of the accretion disc and the NS spin. For the poloidal field component, we adopted one of the configurations discussed by Wang (1995), where  $B_{\phi}$  is limited by diffuse decay due to turbulent mixing within the disc:

$$B_z = -\eta \frac{\mu}{R^3} \quad (11)$$

$$B_{\phi} = B_z \frac{\gamma_{\text{disc}}}{\alpha_{\text{disc}}} \frac{\Omega - \Omega_K}{\Omega_K}, \quad (12)$$

where  $\eta \leq 1$  is a screening coefficient which is constant over a wide range of  $R$ , and we assumed to be equal to 0.2, according to Ghosh & Lamb (1979a),  $\mu$  is the NS magnetic moment,  $B_{\phi}$  is the poloidal component of the magnetic field in the upper surface of the accretion disc (in the lower surface, it has the same magnitude and opposite direction),  $\gamma_{\text{disc}} \approx 1$  is a numerical factor that describes the transition in the  $z$ -direction between the Keplerian motion (inside the accretion disc) and the corotation with the NS (outside of the disc) (for more details, see Ghosh & Lamb 1979b; Wang 1995),  $\alpha_{\text{disc}}$  is the viscosity parameter (we assumed = 0.05, according to Penna et al. 2013),  $\Omega$  is the angular velocity of the NS,  $\Omega_K$  is the Keplerian angular velocity of the accretion disc. We assumed that the strength of the poloidal field component varies linearly within the disc from  $B_{\phi}$  (upper surface) to  $-B_{\phi}$  (lower surface). Inside the disc, we neglected any effect of advection of the field inward (thus any additional radial component of the magnetic field), due to the accretion of matter (see, e.g., Jafari & Vishniac 2018).

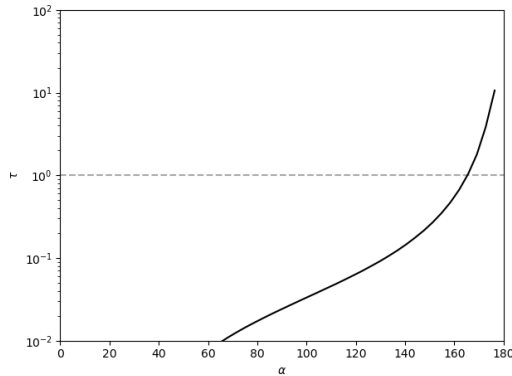


**Figure 7.** The optical depth for a  $\gamma$ -ray photon with energy  $E_\gamma = 1$  TeV injected with an angle  $\alpha$  in the photon field of the donor star (see also Appendix B).

## 2.4 Cascades

Some of the primary photons produced inside the accretion disc can traverse the entire disc without undergoing any interaction. The others produce cascades of  $e^\pm$  pairs and photons, until they escape from the disc. Similarly, outside of the accretion disc, photons, electrons, and positrons can produce cascades, until they possibly reach the observer or achieve an energy which is not relevant for our calculations ( $< 10$  GeV). The processes involved in the cascades we considered are:

- i) pair production in the Coulomb field of nucleus;
- ii) pair production in photon-photon collisions;
- iii) magnetic pair production;
- iv) bremsstrahlung;
- v) inverse Compton;
- vi) synchrotron and curvature.

The fields of soft photons that can interact with  $e^\pm$  and  $\gamma$ -ray photons can be roughly limited to three: the photons from the accretion disc, those emitted by the companion star, and the Extragalactic Background Light (EBL). To have a general idea on the influence of these photon fields on the development of cascades in an XRB, we calculated their numerical density in the vicinity of the NS. For the spectrum emitted by the accretion disc, we considered the standard model of the multi-temperature blackbody spectrum of a thin accretion disc (see, e.g., [Frank et al. 2002](#), and references therein) and we assumed a NS with mass  $M_{\text{NS}} = 1.4 M_\odot$ , radius  $R_{\text{NS}} = 12$  km, X-ray luminosity  $L_x = 10^{37}$  erg s $^{-1}$  and  $B = 10^{12}$  G (at the poles). For the spectrum emitted by the donor star surface, we assumed a simple blackbody model with  $T_{\text{eff}} = 25000$  K, radius  $R_d = 11 R_\odot$ , and orbital separation  $a = 1.6 \times 10^{13}$  cm (roughly corresponding to  $P_{\text{orb}} = 100$  d for a typical Be star). The density of photons from the accretion disc at an equatorial distance from the NS and height from the equatorial plane of the disc equal to  $R_0$  is  $\approx 10^{13}$  cm $^{-3}$ , about a factor  $\sim 30$  larger than that of the photon field from the companion star. This factor shows substantial source-to-source variability: it is primarily affected by the properties of the accretion disc and the separation between the two stars. The influence of the photon field emitted by the donor star on the development of the cascades was investigated extensively by [Bednarek \(1997, 2000\)](#), and [Sierpowska & Bednarek \(2005\)](#). They showed that when the radiation field from the donor star is taken into account, the observed  $\gamma$ -ray emission might show an orbital modulation. This is due to the anisotropic radiation field produced by the donor star through which the  $\gamma$ -ray radiation propagates, and the fact that the intensities of the secondary  $\gamma$ -rays depend on the angle of observation measured from the direction of propagation of the photons defined by the place of injection of the  $\gamma$ -rays (the NS) and the origin of the soft photons (the donor star). To further evaluate the possible influence of the donor star radiation on the evolution of the cascade, we followed a method similar to that described in [Bednarek \(1997\)](#) to compute the optical depth for the propagation of  $\gamma$ -ray photons in the donor star photon field as a function of the angle of the  $\gamma$ -ray photon injection  $\alpha$  (see Appendix B). Assuming that the donor star emits blackbody radiation, and assuming the same values for  $T_{\text{eff}}$ ,  $R_d$ , and  $a$  as above, we find that the optical depth is low over a wide range of angles  $\alpha$  (Fig. 7). Hence, in our calculations we do not take into account the effects of the donor star radiation field on the observed  $\gamma$ -ray emission, preferring a more streamlined approach to highlight the key aspects of the evolution of the cascades influenced by the physical processes more closely related to the NS itself and its immediate environment. On the other hand, future developments of this model will be important to incorporate the effects of the interactions with the photon field of the donor star, to further explore their potential impact on the overall  $\gamma$ -ray emission. [Bednarek \(1997\)](#) showed that these have a significant influence on the cascades for binary systems with smaller orbital separations than those considered here. The significantly lower density of photons in the EBL (see, e.g., [Cooray 2016](#)) shows that they have a negligible impact on the development of cascades in Galactic XRBs. For instance, when considering  $\gamma$ -ray photons with energies of the order of TeV, the mean free path for  $\gamma\gamma \rightarrow e^{+/-}$  interactions (with EBL photons) is approximately 100 Mpc (see, for example, [De Angelis et al. 2013](#); [Berezinsky & Kalashev 2016](#)).

Cascades are calculated in the work presented here using Monte Carlo simulations, in a framework based on that presented in [Protheroe](#)



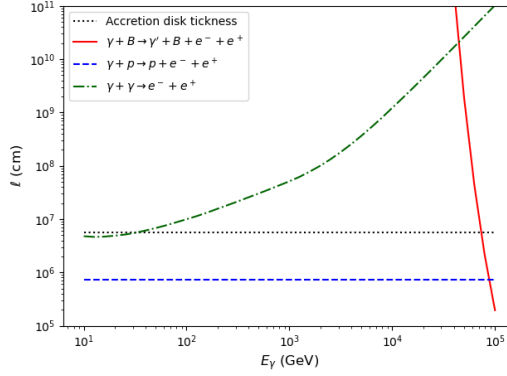


**Figure 8.** An example of possible interaction lengths as a function of the  $\gamma$ -ray photon energy, inside the disc.

(1986). This is one of the various computational and analytical techniques that have been proposed to describe the evolution and output of cascades in astrophysical objects. For alternative methods see, among the others, Aharonian & Plyasheshnikov (2003) and Berezhinsky & Kalashev (2016). Figure A1 in Appendix A provides a general outline of the procedure used in our study to calculate the observed  $\gamma$ -ray emission and in particular to simulate the cascades.

The *first step* (see Fig. A1) of these calculations is to provide a list of input parameters to describe the properties of the binary system to be studied. These are: the X-ray luminosity, the magnetic field intensity at the polar cap, the distance of the binary system from the observer, the type of shielding in the accelerating gap (strong or weak), and the number of  $N$  primary photons to simulate.

The *second step* involves the acceleration of protons and the production of primary photons. The analytical calculations are described in Sections 2.1 and 2.2. For each of the  $N$  primary photons, the position, energy, and direction are simulated. For a given proton accelerated in the gap, which is assumed to enter perpendicularly in the accretion disc (due to the “aligned rotator” assumption), its radial distance from the NS,  $R$ , is sampled from a uniform distribution in the range  $R_0 - R_A$  (Anchordoqui et al. 2003). For a given input X-ray luminosity  $L_x$  and the radial distance  $R$  just sampled, the proton density (from the standard accretion disc structure equations), the potential drop (Eqs. 1 or 4), and the cross section of inelastic  $pp$  collision (Eq. 7) are calculated. Then, the height  $h$  in the region of the disc where the  $\pi^0$  decay occurs is determined by sampling the path of the proton from an exponential distribution with mean free path (see, e.g., Protheroe 1986, for the details of this type of calculations). The energy of the primary photon is then sampled from the energy distribution of photons from  $\pi^0$  decay, in the range  $E_{\text{inf}} - E_{\text{sup}}$ . The direction of the primary photons ( $\theta$ , where  $\theta = 0$  corresponds to the direction normal to the accretion disc plane) is sampled using the aberration light formula in the accretion disc rest frame (see, e.g., Rybicki & Lightman 1979).

*Third step:* inside the accretion disc. Primary photons can start cascades through different processes. For each process, the pairs or photons produced have energies and directions sampled from the respective distributions laws. For pair production in Coulomb field nucleus we used the Davies-Bethe-Maximon formula for screened point nucleus for extreme relativistic energy (Motz et al. 1969). For pair production in photon-photon collisions inside the accretion disc, we adopted the treatment of Protheroe (1986). For magnetic pair production we used the treatment of Erber (1966) and Daugherty & Harding (1983). For each photon, given the local conditions in the accretion disc (see Sect. 2.3), the pair production process that dominates over the others is selected by comparing the interactions lengths sampled by the characteristic distribution of each pair production process. Figure 8 shows possible interaction lengths for different pair production processes as a function of the  $\gamma$ -ray photon energy, inside the disc. They are obtained assuming  $L_x = 5 \times 10^{37}$  erg s $^{-1}$ ,  $B = 5 \times 10^{12}$  G (at the polar cap),  $\gamma$ -ray photon located at a distance  $R_A$  from the NS and with a direction perpendicular to the magnetic field line. Figure 8 has to be considered just as an example: the exact position and directions of the  $\gamma$ -ray photons,  $L_x$ , and the properties of the local magnetic field affect the mutual values of the interaction lengths on a case-by-case basis. Electrons and positrons can interact with the environment (protons in the disc, photons, and magnetic field) to produce secondary photons. For the inverse Compton scattering of soft photons produced by the accretion disc, with interactions within the disc, we adopted the treatment of Protheroe (1986). The inverse Compton scattering and photon-photon interactions occurring outside of the accretion disc involve the spatially varying anisotropic field of the soft photons emitted by the accretion disc. Protheroe et al. (1992, and references therein) showed that in this case, the properties of the pair-Compton cascades differ substantially from the cascade calculations based on an isotropic field of soft photons. Outside of the accretion disc (*fourth step*, see Fig. A1), the  $\gamma$ -ray photons and electrons which escape from the disc interact with the accretion disc soft photons mainly through “tail-on” collisions, which influences the shape of the emerging  $\gamma$ -ray spectrum. Therefore, for these processes outside of the accretion disc we followed the treatment described in Protheroe et al. (1992), that is, a modified version of the calculation method described in Protheroe (1986), better suited to the varying anisotropic radiation field. For bremsstrahlung, we used the treatment for complete screening and relativistic electrons described in Jackson (1975). For synchrotron, we adopted the formulation presented in Berestetskii et al. (1982) that takes into account the quantum effects for relativistic electrons in strong magnetic fields. As pointed out, for example by Vietri (2008), synchrotron radiation from an electron in a strong magnetic field dissipates efficiently the component of its energy perpendicular to the magnetic field line. We therefore assumed that

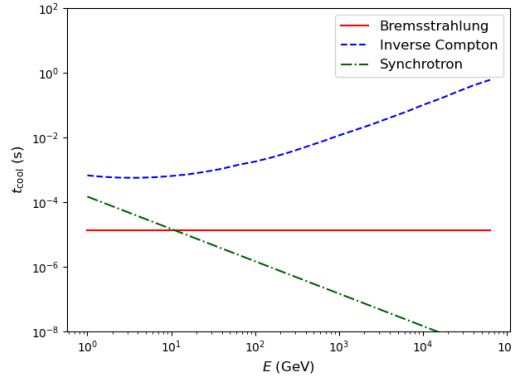


**Figure 9.** An example of possible cooling times as a function of the electron energy, calculated inside the disc.

after the emission of synchrotron radiation, the electrons follow the magnetic field line. For curvature radiation, we considered the classical treatment (e.g., Vietri 2008) and Ochelkov & Usov (1980) for the curvature radius of a dipole magnetic field. We neglected the curvature inside the disc because it depends on the complicated structure of the magnetic field lines inside it, and its effect is in general small compared to bremsstrahlung and synchrotron. Similarly to Orellana et al. (2007), by comparing the cooling times of these processes, we determined in each case which one dominates. Figure 9 shows an example of the cooling times of different processes as a function of the electron energy, calculated inside the accretion disc. We assumed  $L_x = 10^{37}$  erg s $^{-1}$ ,  $B = 10^{12}$  G (at the polar cap), the electron at a distance  $R_A$  from the NS and its trajectory perpendicular with respect to the magnetic field line. Different locations and directions of the electron, as well as different values of  $L_x$  and  $B$  affect significantly the mutual values of the cooling times, which are thus calculated in the simulations on a case-by-case basis. At each stage of the photon and particle production in the cascade, the new position  $(R, h)$  is calculated as described in Protheroe (1986), by sampling from an exponential distribution with mean equal to the interaction length, and subsequently by adding the the obtained value to the path travelled by cascade that originated it. In our calculations, we allowed the cascade to continue developing until the particle or photon energy reaches energies below 10 GeV or the distance travelled by the cascade is lower than the distance of the source from the observer. When the photon exceeds this distance, its energy and direction are released as output.

### 3 RESULTS

#### 3.1 Contribution of different interaction processes to the $\gamma$ -ray spectrum

Table 2 and Fig. 10 show the observable  $\gamma$ -ray luminosities and spectra (above 10 GeV) calculated assuming a strongly shielded gap, for three different X-ray luminosities, and for different types of interaction processes activated. Specifically, Fig. 10 shows the  $\gamma$ -ray spectra from photons that escaped from the accretion disc, those observed (i.e. photons that escaped from the disc and survived along their journey between the source and the observer and photons that have transformed into other photons, through cascades that have occurred outside the disc), and the spectrum of the primary photons (those created by the  $\pi^0$  decay inside the disc). Figure 11 shows, for each of the simulations displayed in Fig. 10, how the cascade of  $\gamma$ -ray photons develops inside and outside the disc. “Gen” (generation) 1 corresponds to primary photons, i.e. those produced by the decay of  $\pi^0$ . The photons of second generation are produced by the  $e^\pm$  pairs which were, in turn, produced by primary photons. The names of the other generations of photons (gen  $\geq 2$ ) follow the same scheme. The results for the weakly shielded gap are in Sect. C. Left panels in Fig. 10 (and left columns in Table 2) show the spectra (and luminosities) obtained when only the interaction processes involving the nuclei are activated (pair production in the Coulomb field of nucleus and bremsstrahlung). Being the region outside of the accretion disc poor of nuclei, (indeed, they are neglected in our simulation), in the spectra of this column the “escaped” spectrum coincides with the “observed” spectrum. The spectra in the central column are obtained including, in addition to the interaction processes of the left column, also those involving the interactions with the photons produced in the accretion disc (pair production in photon-photon collisions and Inverse Compton scattering). The right column shows spectra obtained when also the processes that involve the interaction of  $e^\pm$  and  $\gamma$ -ray photons with the magnetic field are considered (magnetic pair production, synchrotron, curvature). The spectrum of primary photons is modified mostly by the interactions of photons and  $e^\pm$  with the nuclei of the disc. When  $L_x$  increases, the density of nuclei and the height of the disc in the region of interest for the  $\gamma$ -ray production ( $R_0 - R_A$ ) increases, and therefore so does the number of interactions. Because of it, primary photons lose more energy and produce more pairs and secondary photons with softer energies (Fig. 11). Observing Table 2, the peak of secondary photons produced by bremsstrahlung is reached, for the specific case explored here, when  $L_x \approx 10^{37}$  erg s $^{-1}$ . For higher values of  $L_x$ , the spectrum becomes softer, due to the more complex cascades that develop inside the disc. When the processes involving interactions with the soft photons from the accretion disc are activated, the most affected spectra are those observed. The denser is the field of soft photons emitted by the accretion disc, the larger will be the suppression of  $\gamma$ -ray photons due to the production of pairs. When also the interactions of  $e^\pm$  and photons with the magnetic field are considered, the escaped and observed  $\gamma$ -ray radiation are further suppressed.

**Table 2.**  $\gamma$ -ray luminosities ( $\geq 10$  GeV), for the primary photons ( $L_{\text{pri}}$ ), photons which escaped from the disc ( $L_{\text{esc}}$ ), and photons which reached the observer ( $L_{\text{obs}}$ ), assuming strong shielding, for different X-ray luminosities, and for different radiation and pair processes activated. We assumed  $B = 4 \times 10^{12}$  G (i.e. a framework compatible with the Be/XRB A0535+26).

$L_x$	$L_\gamma$	Case A <sup>a</sup>	Case B <sup>b</sup>	Case C <sup>c</sup>
		nuclei	nuclei + photons	nuclei + photons + $\vec{B}$
		erg s <sup>-1</sup>	erg s <sup>-1</sup>	erg s <sup>-1</sup>
$5 \times 10^{36}$	$L_{\text{pri}}$	$6.9 \pm 0.4 \times 10^{34}$	$7.3 \pm 0.4 \times 10^{34}$	$7.0 \pm 0.4 \times 10^{34}$
	$L_{\text{esc}}$	$5.3 \pm 0.2 \times 10^{34}$	$5.6 \pm 0.2 \times 10^{34}$	$4.4 \pm 0.2 \times 10^{34}$
	$L_{\text{obs}}$	$5.3 \pm 0.2 \times 10^{34}$	$4.2 \pm 0.2 \times 10^{34}$	$2.5 \pm 0.2 \times 10^{34}$
$10^{37}$	$L_{\text{pri}}$	$1.76 \pm 0.10 \times 10^{35}$	$1.77 \pm 0.09 \times 10^{35}$	$1.75 \pm 0.09 \times 10^{35}$
	$L_{\text{esc}}$	$9.8 \pm 0.4 \times 10^{34}$	$9.9 \pm 0.4 \times 10^{34}$	$5.0 \pm 0.3 \times 10^{34}$
	$L_{\text{obs}}$	$9.8 \pm 0.4 \times 10^{34}$	$4.6 \pm 0.4 \times 10^{34}$	$1.7 \pm 0.2 \times 10^{34}$
$5 \times 10^{37}$	$L_{\text{pri}}$	$1.39 \pm 0.06 \times 10^{36}$	$1.37 \pm 0.06 \times 10^{36}$	$1.36 \pm 0.05 \times 10^{36}$
	$L_{\text{esc}}$	$2.40 \pm 0.13 \times 10^{34}$	$2.00 \pm 0.12 \times 10^{34}$	$1.2 \pm 0.4 \times 10^{32}$
	$L_{\text{obs}}$	$2.40 \pm 0.13 \times 10^{34}$	$5.8 \pm 2.8 \times 10^{32}$	–

<sup>a</sup> Case A: interaction with nuclei: pair production in the Coulomb field of nucleus and bremsstrahlung.

<sup>b</sup> Case B: interaction with nuclei and photons from the accretion disc: pair production in the Coulomb field of nucleus, pair production in photon-photon collisions, bremsstrahlung, inverse Compton with soft photons from the accretion disc.

<sup>c</sup> Case C: interaction with nuclei and photons from the accretion disc, and with the magnetic field: pair production in the Coulomb field of nucleus, pair production in photon-photon collisions, magnetic pair production, bremsstrahlung, inverse Compton with soft photons from the accretion disc, synchrotron, and curvature.

### 3.2 $L_\gamma$ with respect to $L_x$ , magnetic field strength, and type of gap shielding

We explored the properties of the  $\gamma$ -ray emission for different values of the X-ray luminosity ( $L_x$ ), the magnetic field strength at the poles ( $B$ ), and for strong and weak shielding of the gap. The resulting  $\gamma$ -ray luminosities ( $L_\gamma$ ) are shown in Fig. 12, while some sample spectra (“escaped” from the disc and “observed”) are shown in Fig. 13. In general,  $L_\gamma$  increases with  $L_x$ , it reaches a peak, and then starts to decrease. This trend is seen both in the  $\gamma$ -ray emission that escapes from the disc and in the one that is observed. The rise branch of  $L_\gamma$  depends mostly on the properties of the accelerating mechanism (Sect. 2.1), which produces more protons (and consequently primary photons) when  $L_x$  increases. The decay branch is caused by the loss of energy due to the formation of more complex cascades that reduce the number of photons with very high energy. The  $\gamma$ -ray luminosities for the weakly shielded gap are  $\sim 10^3 - 10^4$  times lower than for strongly shielded gaps, due to the lower energy achieved by the primary photons (Figs. 3 and 6). Figure 12 also shows that when  $B$  increases, the rise branch has a lower  $L_\gamma$  and the peak is reached at higher  $L_x$ . The lower  $L_\gamma$  in the rise branch as  $B$  increases is due to the dependence of  $J_{\text{max}}$  with the magnetic field strength (see Eq. 5 and Fig. 4). To understand the shift of the peak of  $L_\gamma$  to larger  $L_x$ , we have to recall that as  $B$  increases, the region of the disc hit by accelerated protons,  $R_0 - R_A$ , is further away from the NS. As the distance from the NS increases,  $n_p$  (inside the disc) decreases. Therefore, for a given  $L_x$ , when  $B$  increases, the cascades in  $R_0 - R_A$  are less developed because less interactions occur: the initial energy of the primary photons is less distributed to  $e^\pm$  and photons of higher generations and lower energies. Therefore, when  $B$  increases, it is necessary to increase  $L_x$  to push the region  $R_0 - R_A$  inwards, where  $n_p$  and the field of X-ray photons from the disc are sufficiently high to produce a more complex cascade that reduces the flux of  $\gamma$ -ray photons.

Figure 13 shows some examples of the different shapes of the observable spectra obtained from our simulations, assuming different values of  $L_x$ ,  $B$ , and for strong and weak shielding of the gap. The top left panel shows that, for strong shielding, the spectra are flatter as  $L_x$  increases. This happens because the region where protons hit the disc moves inwards, where  $n_p$  is larger, and therefore more complex cascades are produced. They redistribute the high energies of primary photons to photons having less energies. For strong shielding, when  $B$  increases (and  $L_x$  is fixed, as shown in the bottom left panel of Fig. 13), there are two mechanisms working against each other. The current of accelerated protons (Eq. 5) and their energy (Eq. 1) are inversely proportional to the magnetic field strength. Therefore, the rising branch of the spectrum, that maps the original primary photons spectrum (see also Fig. 10) moves to lower energies. On the other hand, when  $B$  increases, the region where protons hit the accretion disc moves outwards, where  $n_p$  is lower. Therefore, the resulting cascades are less developed and more primary photons (and less photons of secondary or higher generation) are able to escape from the disc, leading to an increase of the observed flux above  $\sim 1$  TeV. This leads to an increase in the slope of the branch. The spectra obtained for the weak shielding case are much softer than those for strong shielding case, again due to the lower energy achieved by the primary photons in the weak shielding case (Figs. 3 and 6). Simulations with magnetic fields of  $10^9$  G and  $10^{10}$  G did not provide any observable photons, due to the higher  $n_p$  in the region  $R_0 - R_A$  of the disc.

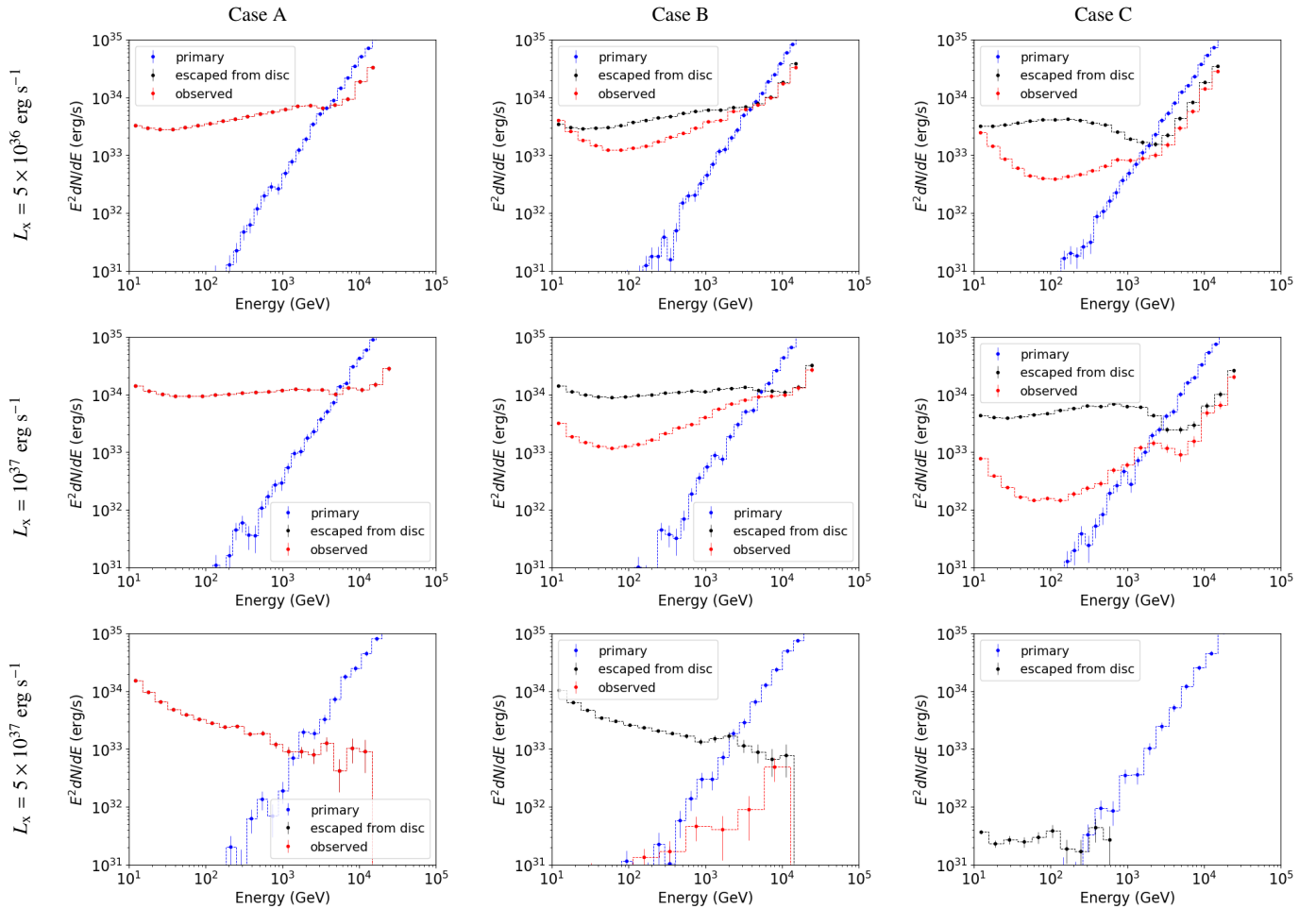


**Figure 10.**  $\gamma$ -ray spectra for the primary photons, photons that escaped from the disc, and photons that reached the observer, for different X-ray luminosities, and for different radiation and pair processes activated, as described in Table 2. We assumed  $B = 4 \times 10^{12}$  G and a strong shielded gap.

### 3.3 Beaming factor

For a bipolar emission, the beaming factor is given by  $f_b \approx 1 - \cos \theta$ , where  $\theta$  is the half-opening angle (with respect to the normal of the accretion disc plane). We calculated, through our simulations,  $f_b$  for different values of the X-ray luminosity and magnetic field strength, assuming strongly and weakly shielded gap and a cone-beam that contains 90% of the total emitted  $\gamma$ -ray radiation. The results are shown in Fig. 14. The panel for strong shielding in the figure shows that  $f_b$  increases with  $L_x$ , until it reaches a maximum. The point where  $f_b$  starts to decrease occurs at higher X-ray luminosities as the magnetic field increases. These trends can be explained as follows. When  $L_x$  is low ( $\lesssim 10^{35-36} \text{ erg s}^{-1}$ ), the density and height of the disc in the region where the accelerated protons hit the disc ( $\sim R_0 - R_A$ ) are relatively small. Most of the primary photons escapes from the disc without further interactions. Therefore, the beaming factor is small (nearly zero at very low  $L_x$ , due to the initial assumptions of aligned rotator and that protons enter perpendicularly in the accretion disc). When  $L_x$  increases, the primary photons interact more inside the accretion disc, first producing  $e^\pm$  pairs, then secondary photons (and, eventually, higher generations). A substantial fraction of  $e^\pm$  starts to be bended by the poloidal magnetic field inside the disc, and the directions of the secondary photons plus the primary photons that escaped from the disc will thus cover a wider angle. When  $L_x$  increases further, the density and thickness of the disc increases such that a more complex cascade develops inside the disc. The  $e^\pm$  pairs that are created at each step of the cascade will more closely follow the direction of the magnetic field lines inside the disc. The emerging beam of radiation will thus start to become narrower again.

For a given  $L_x$ , the region where protons hit the disc ( $\sim R_0 - R_A$ ) moves outwards as the magnetic field strength increases. Moving towards the outermost regions,  $n_p$  decreases. Therefore, for  $L_x \gtrsim 5 \times 10^{36} \text{ erg s}^{-1}$ , when the magnetic field strength increases, the cascades inside the disc are less developed and for the above reasons,  $f_b$  increases. The right panel of Fig. 14, which shows for the weak shielding case, covers a smaller range of X-ray luminosities compared to the left panel. We have shown previously this behaviour (see, e.g., Fig. 12). In the weak shielding case, indeed, the  $\gamma$ -ray emission is much lower than in the strong case. In this case, the ability to simulate  $\gamma$ -ray photons for low and high X-ray luminosities (i.e., when the source is expected to be very faint in the  $\gamma$ -ray band) is highly reduced, since extremely computationally demanding simulations would be required. The right panel of Fig. 14 shows that  $f_b$  does not show a significant variability within the uncertainties. It shows also an overall lower  $f_b$  than in the case of strong shielding. This can be explained with the lower number

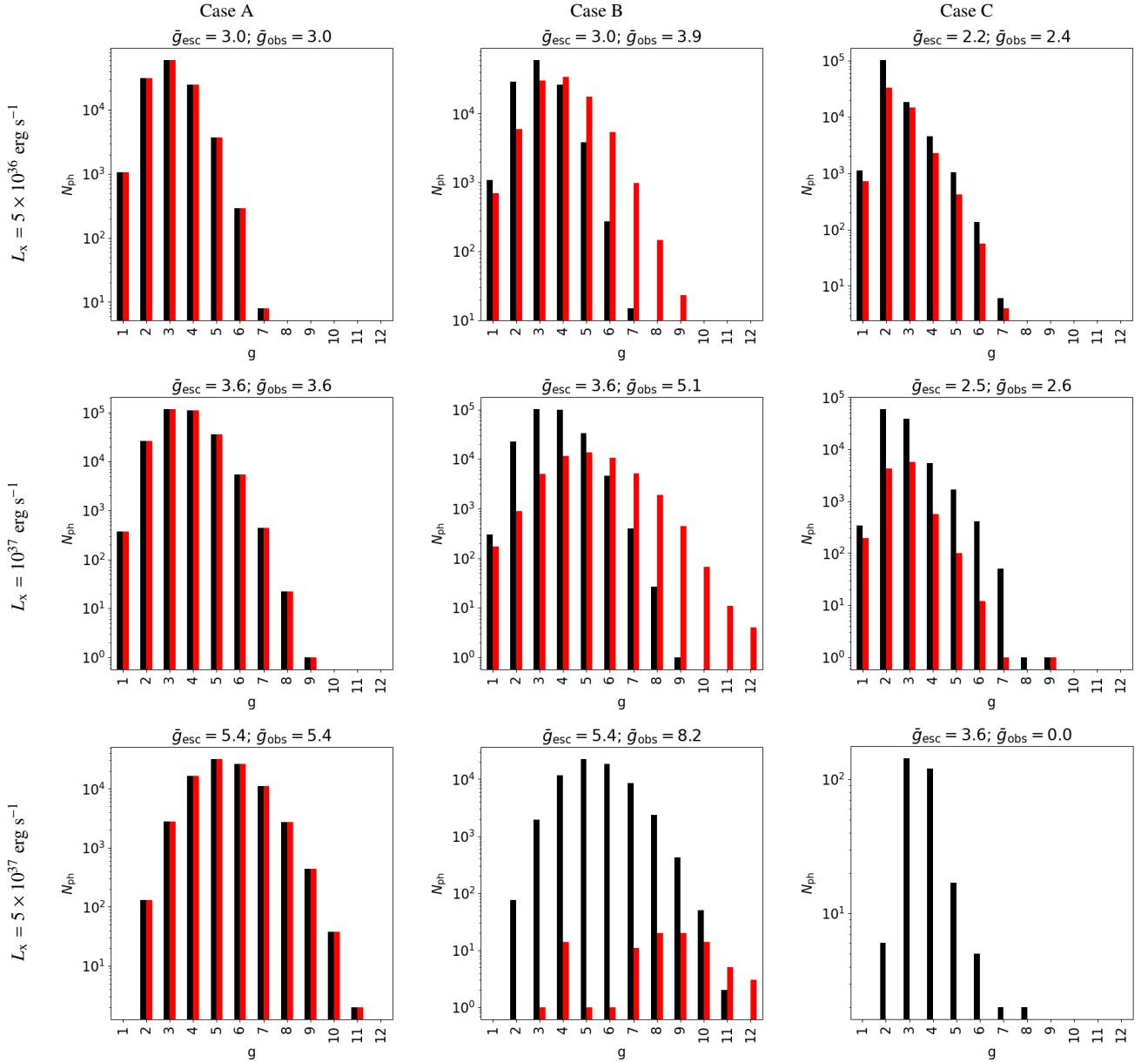


**Figure 11.** Histograms of the generations of photons that escape from the disc (black histogram) and reach the observer (red histogram), for different X-ray luminosities and radiation and pair processes activated as described in Table 2. We assumed  $B = 4 \times 10^{12}$  G and a strong shielded gap. On top of each panel is shown the average value of the generation number for photons that escaped the disc ( $\bar{g}_{\text{esc}}$ ) and those that reached the observer ( $\bar{g}_{\text{obs}}$ ).

of interactions in the weak shielding scenario (see Fig. C2, compared to Fig. 11), which leads to photons with smaller deviations from the original trajectory of the primary photons (which are almost perpendicular to the disc plane).

#### 4 DISCUSSION

In Sect. 3 we showed that, in the framework of the model presented in this work, HMXBs, which typically have magnetic fields of  $B \approx 10^{12} - 10^{13}$  G, are potentially bright  $\gamma$ -ray sources. High X-ray luminosities and low magnetic fields favour the production of high rates of protons with high energy (see Figures 3, 4, 5, 6). Therefore, NS-LMXBs, which have typically low magnetic field strength ( $B \approx 10^8 - 10^{10}$  G), observed during outbursts ( $L_x \approx 10^{36} - 10^{37}$  erg s $^{-1}$ ), could also be bright  $\gamma$ -ray sources. On the other hand, when a NS with low magnetic field is bright in X-rays, the density in the  $R_0 - R_A$  region of the accretion disc is larger and reduces most of the escaping  $\gamma$ -ray photons. In this regard, we performed simulations assuming  $L_x = 3 \times 10^{36}$  erg s $^{-1}$ , for strong and weak shielding for the gap, and  $B = 10^9$  G and  $B = 10^{10}$  G which did not produce any emission of  $\gamma$ -ray photons able to escape from the accretion disc. Harvey et al. (2022a) pointed out that, although the population of LMXBs in our Galaxy is almost twice than that of HMXBs, its members are only half as many in the latest

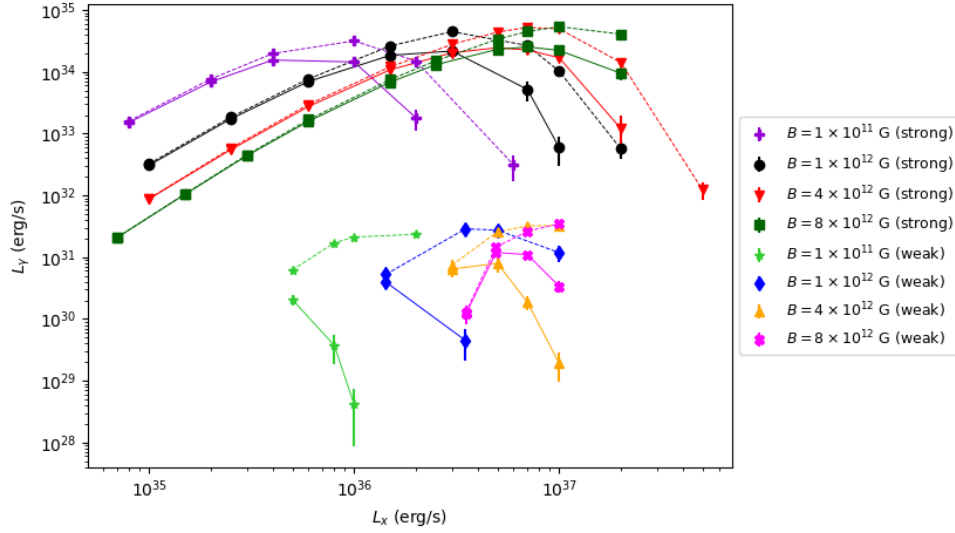


**Figure 12.**  $\gamma$ -ray luminosities with respect to the input X-ray luminosity for different magnetic field strengths, strong and weak shielding, and for photons escaped from the disc (dashed lines) and photons that reached the observer (solid lines).

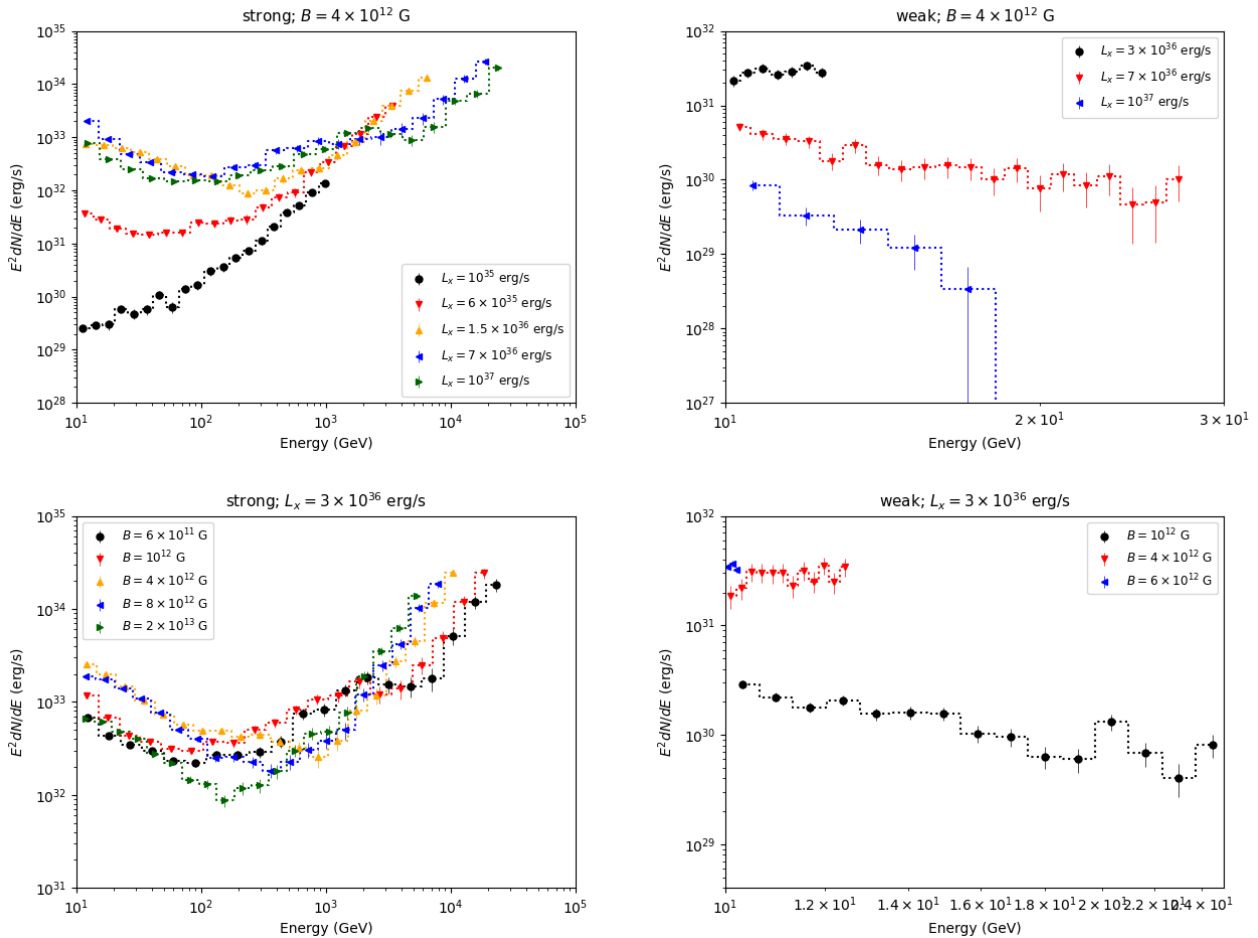


**Figure 13.**  $\gamma$ -ray spectra of photons which reached the observer, for different luminosities (left panels) and magnetic field strengths (right panels), assuming strong (upper panels) and weak (lower panels) shielding.

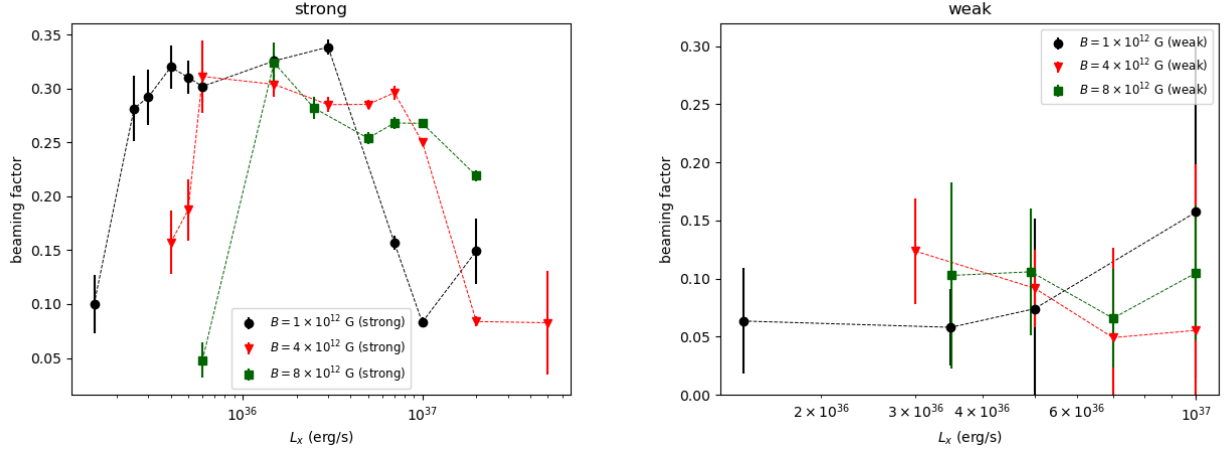


**Figure 14.** Beaming factor as function of the X-ray luminosity, for three different values of the magnetic field strength, assuming strong (left panel) and weak (right panel) shielding.

*Fermi* catalogue, and consists of only four sources. In addition, many LMXBs are contained in globular clusters, which are too crowded to allow a simple identification. For these reasons, hereon we focus on HMXBs.

#### 4.1 Observability of HMXBs in the $\gamma$ -ray band

We assess the observability of HMXBs above 10 GeV assuming that the model developed in Sect. 2 is the only one possible for the production of  $\gamma$ -rays in HMXBs. Given the number of HMXBs currently known in our Galaxy, we calculate the fraction of them that could be observable by *Fermi*/LAT and the Cherenkov Telescope Array Observatory (CTAO). We consider the *Fermi*/LAT sensitivity in the  $\sim 10$ –100 GeV band (after 4 years of survey) and that expected for CTA in the  $\sim 0.1$ –100 TeV band (after 50 hours of observations<sup>3</sup>). To date, we know in our Galaxy  $\sim 54$  Be/XRBs and 32 HMXBs with OB supergiant stars (Neumann et al. 2023; Fortin et al. 2023; Arnason et al. 2021; Liu et al. 2006). For some Be/XRBs, there are indications that during X-ray outbursts, an accretion disc forms around the pulsar (e.g. from the observation of QPOs, from the properties of the spin period variability as function of the mass accretion rate, and from the detection of double peaked He II  $\lambda 4686$  emission lines; see, e.g., Hayasaki & Okazaki 2004, Motch et al. 1991, Rajoelimanana et al. 2017, and references therein). For HMXBs with supergiant companion, instead, the presence of an accretion disc is less certain. In general, it seems that in most of these systems the accretion is spherically symmetrical, likely not mediated by a standard accretion disc (see., e.g., Davidson & Ostriker 1973). Nonetheless, El Mellah et al. (2019) showed that in some of these systems, a disc-like structure may form around the NS. Since the model we have developed requires the presence of a standard accretion disc, we restrict to the Be/XRBs for the observability calculations. In Sect. 3 we showed that the maximum  $\gamma$ -ray luminosity ( $L_\gamma \approx 10^{33} - 10^{34}$  erg s<sup>-1</sup>) is reached when the X-ray luminosity is  $L_x \approx 10^{36} - 10^{37}$  erg s<sup>-1</sup>. This X-ray luminosity is observed in Be/XRBs during the rise or decay time of a giant outburst, or during normal outbursts (see, e.g., Reig 2011). The sensitivity of a 50-hours observation by CTA in the energy band  $\sim 0.1 - 100$  TeV is  $F_{\text{th}}^{\text{CTA}} \approx 2 \times 10^{-13}$  erg cm<sup>-2</sup> s<sup>-1</sup>. For *Fermi*/LAT, the sensitivity threshold in the energy band  $\sim 10 - 100$  GeV (for  $\sim 1$  year of observations) is  $F_{\text{th}}^{\text{Fermi}} \approx 2 \times 10^{-12}$  erg cm<sup>-2</sup> s<sup>-1</sup>. Therefore, the maximum distances that a Be/XRB can have to be detected by CTA and *Fermi*/LAT are  $d_{\text{th}}^{\text{CTA}} = \sqrt{L_\gamma / (4\pi F_{\text{th}}^{\text{CTA}})} \approx 6.5$  kpc and  $d_{\text{th}}^{\text{Fermi}} \approx 2$  kpc. In both cases, we assumed a conservative  $L_\gamma \approx 10^{33}$  erg s<sup>-1</sup>. The fraction of Be/XRBs within these distances are  $f_{6.5 \text{ kpc}}^{\text{Be/XRB}} \approx 0.7$  and  $f_{2 \text{ kpc}}^{\text{Be/XRB}} \approx 0.2$ . The fraction of Be/XRBs that have shown X-ray luminosities of  $L_x \approx 10^{36} - 10^{37}$  erg s<sup>-1</sup> during transient events are  $f_t \approx 0.6$ . The beaming effect can greatly reduce the number of detectable XRBs in  $\gamma$ -rays, enabling the detection only of those that emit the radiation close to the line of sight. Assuming  $f_b \approx 0.3$  (i.e. roughly the beaming factor expected for  $L_x \approx 10^{36} - 10^{37}$  erg s<sup>-1</sup>, see Fig. 14), we have, for the energy band  $\sim 0.1 - 100$  TeV:  $N_{\text{obs}}^{\text{CTA}} \approx N_{\text{Be/XRB}} f_t f_{6.5 \text{ kpc}}^{\text{Be/XRB}} f_b \approx 7$ , while for the energy band  $\sim 10 - 100$  GeV  $N_{\text{obs}}^{\text{Fermi}} \approx 2$ . Considering an average outburst rate for each Be/XRB of  $\approx 0.5$  outburst/year<sup>4</sup>, a few tens of  $\gamma$ -ray transient events could be observed by CTAO in the next 10 years. If the gap is strongly shielded, most of the  $\gamma$ -ray flux is emitted in the TeV band, while for the weak shielding case, most of the  $\gamma$ -ray flux is emitted in the  $\sim 10 - 100$  GeV band. Therefore,  $N_{\text{obs}}^{\text{CTA}}$  and  $N_{\text{obs}}^{\text{Fermi}}$  can be seen as the number of observable Be/XRBs in the case of gaps strongly or weakly shielded, respectively.

Recently, the detections of some  $\gamma$ -ray counterpart candidates of HMXBs with *Fermi*/LAT have been reported (Harvey et al. 2022b; Xing

<sup>3</sup> See: [https://www.cta-observatory.org/science/ctao-performance/documentation/Cicerone/Cicerone\\_LAT\\_IRFs/LAT\\_sensitivity.html](https://www.cta-observatory.org/science/ctao-performance/documentation/Cicerone/Cicerone_LAT_IRFs/LAT_sensitivity.html) and [https://fermi.gsfc.nasa.gov/ssc/data/analysis/documentation/Cicerone/Cicerone\\_LAT\\_IRFs/LAT\\_sensitivity.html](https://fermi.gsfc.nasa.gov/ssc/data/analysis/documentation/Cicerone/Cicerone_LAT_IRFs/LAT_sensitivity.html)

<sup>4</sup> Based on the number of outbursts of Be/XRBs detected by *Fermi*/GBM since 2008 and reported in <https://gammaray.nsstc.nasa.gov/gbm/science/pulsars.html>

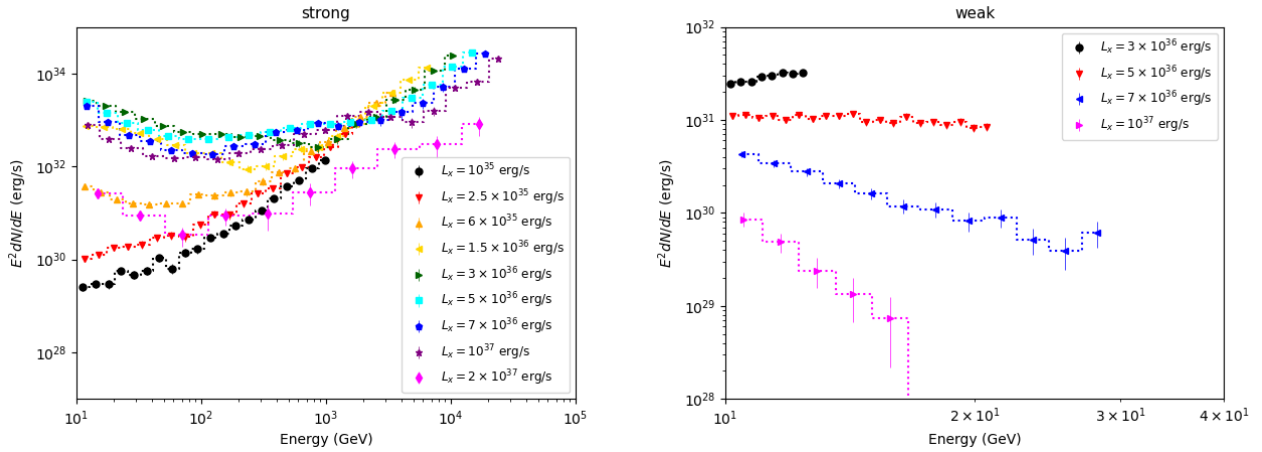


**Figure 15.**  $\gamma$ -ray spectra of A0535+26 for the photons which reached the observer, assuming strong (left panel) and weak (right panel) shielding.

& Wang 2019; Romero et al. 2001; Li et al. 2012, and Table 1). For most of these sources there is no firm detection, or the fundamental parameters of the binary system are unknown (especially the magnetic field strength and the spin period of the pulsar, which are relevant for the mechanism investigated in this paper). We selected two of these sources to perform some tailored simulations. These sources are A0535+26 and GRO J1008–57, two Be/XRBs with known magnetic field strength and spin period. A0535+26 and GRO J1008–57 shows long periods ( $\sim$ years) of low X-ray luminosity states ( $L_x \approx 10^{34} - 10^{35}$  erg s $^{-1}$ ) sporadically interrupted by bright X-ray outbursts with a duration of several days to several weeks, and peak luminosities of  $L_x \approx 10^{38}$  erg s $^{-1}$ . For these two sources there are also some previous observational studies in the  $\gamma$ -ray band, as described below.

#### 4.2 A0535+26

A0535+26 is located at a distance of  $\sim 1.8$  kpc (Bailer-Jones et al. 2021). The pulsar has a spin period of  $\sim 103$  s (Rosenberg et al. 1975) and orbits around the companion star, an O9.7-B0 IIIe type star in  $\sim 111$  days (Coe et al. 2006; Nagase et al. 1982). The magnetic field strength at the poles is rather well known, being measured from the detection of a cyclotron resonance scattering feature (CRSF), with the fundamental line centered at  $\sim 45$  keV (Kendziorra et al. 1994). This energy corresponds to a magnetic field of about  $4 \times 10^{12}$  G (see, e.g., Revnivtsev & Mereghetti 2015). During the 1994 and 1999 giant outbursts, A0535+26 showed broad quasi-periodic oscillations which are considered good indicators of the presence of an accretion disc (see Finger et al. 1996; Camero-Arranz et al. 2012 and references therein) during the outbursts.

Transient  $\gamma$ -ray radiation from a region spatially coincident with A0535+26, on a timescale of months, was detected by EGRET (source name: 3EG J0542+2610; energy band: 30 MeV–10 GeV; Romero et al. 2001; Torres et al. 2001). Romero et al. (2001) discussed the possible counterparts of 3EG J0542+2610 at other wavelengths and then suggested that the only known source within 95% confidence region of the EGRET source able to produce the observed variable  $\gamma$ -ray emission is A0535+26. The  $\gamma$ -ray flux measured with EGRET was  $(14.7 \pm 3.2) \times 10^{-8}$  ph cm $^{-2}$  s $^{-1}$  ( $> 100$  MeV; Romero et al. 2001). Recently, Harvey et al. (2022b) reported a weak correlation between the X-ray and  $\gamma$ -ray fluxes of A0535+26 using 12.5 years of *Fermi*/LAT data (energy band: 0.1–500 GeV). They measured  $\gamma$ -ray emission from A0535+26 (with a significance in the range  $2 < z < 3\sigma$ ) in two bins of the lightcurve, having each time intervals of six months of *Fermi*/LAT data ( $z$  is a statistic measure of the significance of a  $\gamma$ -ray source detection based on the likelihood ratio test; see Harvey et al. 2022b and references therein). These bins roughly correspond to the brightest X-ray outbursts displayed by the source in December 2009 and November 2020. The analysis of *Fermi*/LAT data showed also that most of the  $\gamma$ -ray flux is concentrated in the orbital phase bin  $0.9 \leq \phi < 1$ , that precedes the periastron (significance:  $\sim 3.5\sigma$ ). The *Fermi*/LAT flux is  $\sim 1.45 \times 10^{-6}$  MeV cm $^{-2}$  s $^{-1}$  (0.1–500 GeV). The statistic was too low to extract a spectrum. On the other hand, in a similar data analysis presented by Hou et al. (2023) and based on about 13 years of *Fermi*/LAT observations, A0535+26 is not detected. Hou et al. (2023) suggest that the difference between their findings and those reported by Harvey et al. (2022b) might be due to the different size of the fitting regions adopted, as well as the treatment of the spectral index, which was fixed to different values in Hou et al. (2023) while in Harvey et al. (2022b) it was left free to vary. VERITAS observed A0535+26 at VHEs during the 2009 and 2020 giant X-ray outbursts. In both observational campaigns, the source was not detected. During the 2009 outburst, the flux upper-limit (at the 99% confidence level) was  $F_{u.l.} = 0.5 \times 10^{-12}$  ph cm $^{-2}$  s $^{-1}$  above 0.3 TeV, assuming a power law source spectrum with photon index  $\Gamma = 2.5$  (Acciari et al. 2011). During the 2020 outburst, the preliminary result about the flux upper-limit (99% c.l.) was  $F_{u.l.} = 2 \times 10^{-12}$  ph cm $^{-2}$  s $^{-1}$  above 0.15 TeV, assuming a power law source spectrum with photon index in the range  $\Gamma = 3 - 4$  (Lundy 2021). For the outburst of 2009, Acciari et al. (2011) pointed out that the VERITAS upper-limit is close to the  $\gamma$ -ray flux derived by Orellana et al. (2007) by applying the Cheng & Ruderman (1989) mechanism to A0535+26.

We simulated the  $\gamma$ -ray spectra of A0535+26 for different input values of  $L_x$  (that varies from  $L_x = 10^{35}$  erg s $^{-1}$  to  $L_x \approx 2 \times 10^{37}$  erg s $^{-1}$ ),



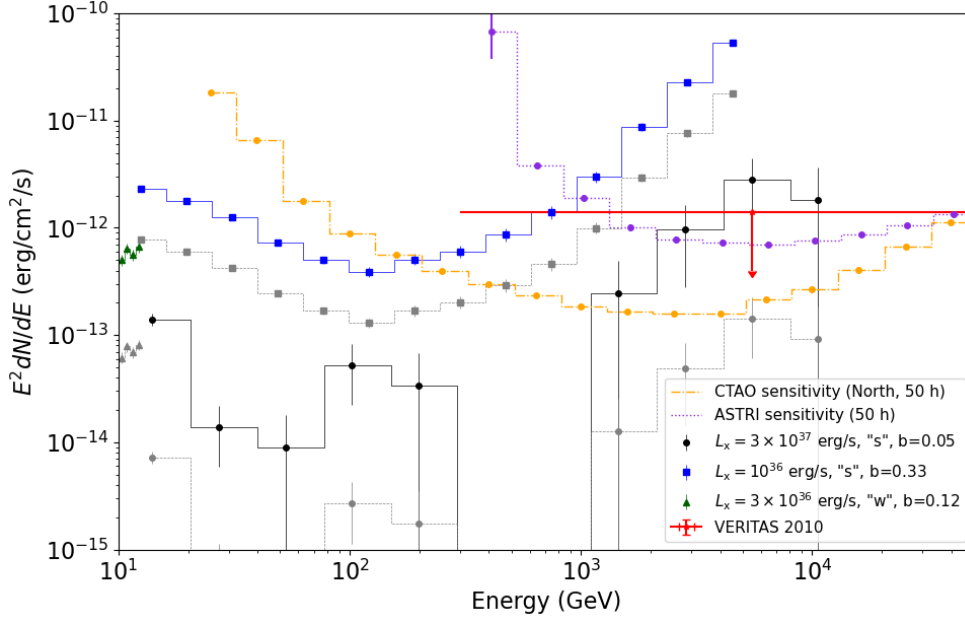


**Figure 16.** Some examples of spectral energy distributions of A0535+26 which take into account the beaming effect, compared with the VERITAS upper-limit measured during the 2009 outburst and apoastron. In gray, the SEDs for no beaming are shown. Orange and blue-violet points show the differential flux sensitivity of the CTAO North and ASTRI Mini-Array, respectively, both for 50 hours of observations.

assuming strong and weak shielding of the gap. The spectra are shown in Fig. 15. These spectra can be used as a grid for comparisons with future observations.

To allow a direct comparison with the available VERITAS upper-limit of the outburst of 2009, we show in Fig. 16 some simulated flux spectra, which take into account the effects of the beaming. The X-ray luminosities of the spectra obtained assuming strong shielding (“s” in the legend of the figure) correspond to the typical average X-ray luminosity during a giant X-ray outburst of A0535+26 ( $L_x \approx 3 \times 10^{37} \text{ erg s}^{-1}$ ) and to the X-ray luminosity measured by Acciari et al. (2011) in the  $\sim 50$  days following the end of the outburst, when the source had an X-ray luminosity of the order of  $L_x \approx 10^{36} \text{ erg s}^{-1}$ . In both time intervals, Acciari et al. (2011) reported the upper-limits for the 0.3–100 TeV flux, which is the same for both X-ray luminosity states and it is shown in the figure. Figure 16 also shows a spectrum obtained assuming weak shielding (“w” in the legend of the figure), for a luminosity state of  $L_x \approx 3 \times 10^{36} \text{ erg s}^{-1}$ . This spectrum is roughly comparable to the *Fermi*/LAT upper-limit obtained by Hou et al. (2023) and with the marginal detection obtained by Harvey et al. (2022b) by averaging about 12 months of data around two giant outbursts ( $\sim 10^{-12} \text{ erg cm}^{-2} \text{ s}^{-1}$  in 10–500 GeV, assuming a power law slope  $\Gamma = 2$  for the energy conversion). If we assume  $L_x \approx 3 \times 10^{37} \text{ erg s}^{-1}$  (s), the  $\gamma$ -ray spectrum is in first approximation compatible with the VERITAS upper-limit, while the  $\gamma$ -ray emission obtained assuming  $L_x \approx 10^{36} \text{ erg s}^{-1}$  (s) is significantly larger than the upper-limit. On the other hand, the soft part of the same spectrum, as well as the spectrum obtained assuming weak shielding are roughly consistent with the *Fermi*/LAT detection. The discrepancy between the simulated spectrum at  $L_x \approx 10^{36} \text{ erg s}^{-1}$  (s) and the VERITAS upper-limit might suggest that the accelerating gap of this source is weakly shielded. Alternatively, if the gap is strongly shielded, other physical processes could be considered for a possible significant impact on the emerging  $\gamma$ -ray emission, especially for  $L_x \approx 10^{36} \text{ erg s}^{-1}$ , for  $\gamma$ -ray emission to fit better with the VERITAS upper-limit. For example, the effects of the UV-optical photons of the donor star might be significant; this possibility was considered by Bednarek (1993, 1997, 2000) and it is not taken into account in our current simulations (see Sect. 2.4). Another parameter that can affect the  $\gamma$ -ray spectrum is the outer radius of the ring where the protons accelerated in the gap hit the accretion disc. We assumed  $R_{\text{out}} = R_A$  (Anchordoqui et al. 2003), but it is not unreasonable to assume a value of  $R_{\text{out}}$  slightly smaller or larger than the Alfvén radius. Another assumption of our simulations that might influence the result is that of aligned rotator. Figure 16 also shows the differential flux sensitivities of the CTAO North and the “Astrofisica con Specchi a Tecnologia Replicante Italiana” (ASTRI) Mini-Array (Scuderi et al. 2022)<sup>5</sup>, both for 50 hours of observations. Future observations of A0535+26 with CTAO and ASTRI Mini-Array will have the adequate sensitivity to test the proposed model and to identify the best ways to improve it.

<sup>5</sup> CTAO data retrieved from <https://www.cta-observatory.org/science/ctao-performance/>. ASTRI Mini-Array data retrieved from figure 4 in Vercellone et al. 2022.

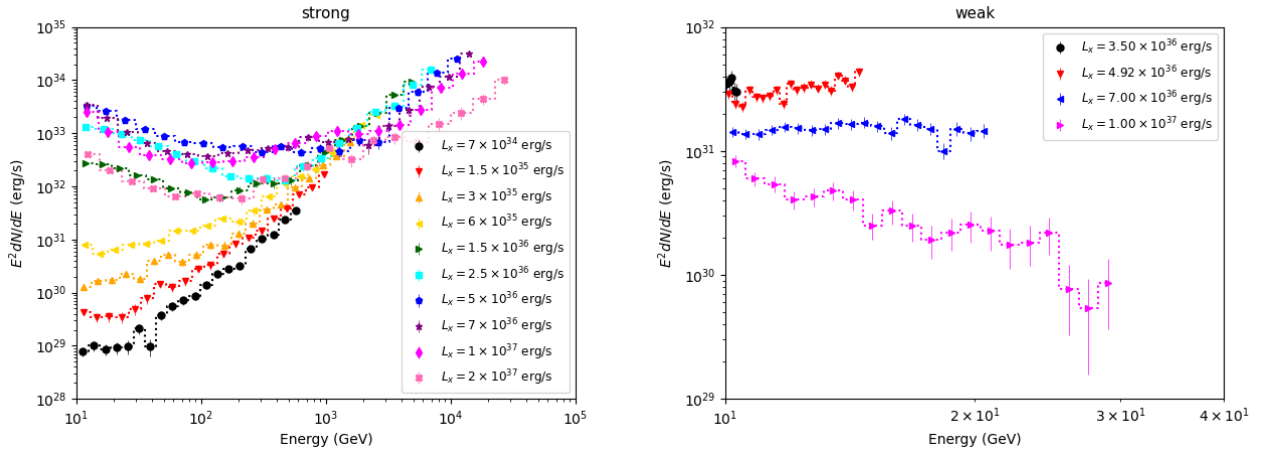


**Figure 17.**  $\gamma$ -ray spectra of GRO J1008–57 for the photons which reached the observer, assuming strong (left panel) and weak (right panel) shielding.

### 4.3 GRO J1008–57

GRO J1008–57 hosts a pulsar with spin period of  $\sim 93.6$  s (Stollberg et al. 1993; Wilson et al. 1994) with an orbital period of  $247.8 \pm 0.4$  d (Levine & Corbet 2006; Coe et al. 2007) and a B1-B2 Ve type donor star (Coe et al. 2007). The magnetic field strength at the poles is one of the highest ever measured through the detection of a CRSF. For this source, there are different detections of CRSFs in the energy range 78–90 keV, which correspond to a magnetic field of about  $7 - 8 \times 10^{12}$  G (Grove et al. 1995; Bellm et al. 2014; Ge et al. 2020). Correlations between the X-ray luminosity and the spin period derivative strongly suggest the presence of an accretion disc around GRO J1008–57 during the X-ray outbursts (see, e.g., Wang et al. 2021). The distance of the system is either  $9.7 \pm 0.8$  kpc or  $5.8 \pm 0.5$  kpc (Riquelme et al. 2012).

Xing & Wang (2019) analysed nine years of *Fermi*/LAT data and used the 4-yr LAT catalogue. They reported the discovery of a transient  $\gamma$ -ray emission spatially coincident with GRO J1008–57. The  $\gamma$ -ray emission is only observed at the orbital phase 0.8–0.9 (where phase 0 is the periastron), and the detection is due mostly to three events, one of which, in 2012–2013, after a giant X-ray outburst. The  $\gamma$ -ray luminosity was  $L_\gamma = 3.6 \times 10^{34}$  erg s $^{-1}$  in 0.5–39 GeV (or  $L_\gamma = 6.7 \times 10^{34}$  erg s $^{-1}$  in 0.1–100 GeV). The X-ray luminosity during the *Fermi*/LAT detections was likely around  $L_x \approx 10^{35}$  erg s $^{-1}$  (Xing & Wang 2019). Harvey et al. (2022b) analysed 12 years of *Fermi*/LAT data. They detected GRO J1008–57 ( $z = 4.9\sigma$ ) with a flux of  $\sim 3.24 \times 10^{-6}$  MeV cm $^{-2}$  s $^{-1}$  (0.1–500 GeV). The lightcurve folded with the orbital period showed excesses at three orbital phases, with two bins consistent with the results of Xing & Wang (2019). Harvey et al. (2022b) do not claim the detection of this source, being all the flux measurements below  $5\sigma$ , but pointed out that it is unlikely that the points with higher flux cluster by chance in phase space.

Similarly to the case of A0535+26, and with the aim of having a spectra grid that can be used for comparisons with future observations, we simulated the  $\gamma$ -ray spectra of GRO J1008–57 for different input values of  $L_x$  (that varies from  $L_x = 10^{34}$  erg s $^{-1}$  to  $L_x = 2 \times 10^{37}$  erg s $^{-1}$ ), assuming strong and weak shielding of the gap. The spectra are shown in Fig. 17. The high  $\gamma$ -ray luminosity reported in Xing & Wang (2019) and Harvey et al. (2022b),  $L_\gamma \approx 10^{34}$  erg s $^{-1}$ , likely corresponding to an X-ray luminosity state of  $L_x \approx 10^{34-35}$  erg s $^{-1}$ , could be roughly explained assuming a strong shielded gap and the  $3\sigma$  upper limit of  $\approx 0.5\%$  for the beaming factor at  $L_x \approx 10^{35}$  erg s $^{-1}$ . For low  $L_x$ , we indeed obtain an upper-limit for  $f_b$  of the order of  $\approx 0.5\%$ .

## 5 CONCLUSIONS AND FUTURE WORK

We explored the properties of the  $\gamma$ -ray emission produced by a pulsar in an XRB, fed by an accretion disc. Our calculations stem from the model presented by CR89 and they take into account several physical processes for the development of photon-electron cascades, inside and outside the accretion disc. Compared to previous works based on CR89, for the cascades we considered more physical processes, which involve interactions with nuclei, soft photons from the accretion disc, and the magnetic field. Compared to the work by Orellana et al. (2007), we have also considered synchrotron, curvature, and magnetic pair production. For the first time, we thoroughly explored the case of “weak shielding” and we considered a more complex configuration for the magnetic fields inside the accretion disc that takes into account the poloidal component. We also presented a wide grid of solutions, which can be used for comparison purposes on many XRBs having a broad spectrum of properties. The grids of solutions are based on different input parameter values of the X-ray luminosity ( $L_x$ ), magnetic field strength ( $B$ ), and for different properties of the region where acceleration occurs, namely “strong” and “weak” shielding in the gap. We explored the parameter space  $8 \times 10^{34} \leq L_x \leq 5 \times 10^{37}$  erg s $^{-1}$ ,  $10^{11} \leq B \leq 8 \times 10^{12}$  G. We found that the  $\gamma$ -ray luminosity spans more than five orders of magnitude, with a maximum of  $\sim 10^{35}$  erg s $^{-1}$ . The  $\gamma$ -ray spectra show a large variety of shapes: some have most of the emission below  $\sim 100$  GeV (weak shielding), others are harder, with emission up to 10–100 TeV (strong shielding). The beaming factor varies from  $\lesssim 0.01$  to  $\sim 0.35$ .

We compared our results with *Fermi*/LAT detections and VERITAS upper-limits of two HMXBs: A0535+26 and GRO J1008–57. More consequential comparisons will be possible when more sensitive instruments will be operational in the coming years, such as, for example, CTAO, ASTRI Mini-Array, the Southern Wide-field Gamma-ray Observatory (SWG0), and the High Energy cosmic Radiation Detection facility (HERD) (Zhang et al. 2014b; Huentemeyer et al. 2019).

The results shown in this work are based on a number of simplifications, which will be addressed in future works. We list the ones we consider most significant. The model by CR89 and our calculations are based on the assumption that the rotational and dipole magnetic axes are aligned. This assumption greatly simplifies the calculations, as demonstrated by other numerous works on pulsars which adopt it. Nevertheless, it is inevitable that our solutions may diverge from those of the more realistic case of an oblique rotator. A similar reasoning applies to the curvature radiation produced within the disc, which we have neglected and could be included in a future work. The interaction effects of the radiation field from the companion star could also be included. Bednarek (1993, 1997, 2000); Sierpowska & Bednarek (2005) showed that if it is taken into account, the observed  $\gamma$ -ray emission can show an orbital modulation. Also the beaming factor can be affected by the assumptions of aligned rotators and the geometry of the magnetic field inside the accretion disc. Therefore, the values reported in this work should be considered within the bounds of the assumptions under which they were derived. Finally, we have considered here only a model, based on the that presented by CR89. In Sect. 1.2 we briefly listed many other models on which work similar to this could be done, and whose importance will become more and more urgent in view of future observational advances in the  $\gamma$ -ray energy band.

## ACKNOWLEDGEMENTS

We thank the anonymous referee for constructive comments that helped to improve the paper. The authors acknowledge support by the High Performance and Cloud Computing Group at the Zentrum für Datenverarbeitung of the University of Tübingen, the state of Baden-Württemberg through bwHPC and the German Research Foundation (DFG) through grant no INST 37/935-1 FUGG. We acknowledge financial contribution from the agreement ASI-INAF I/037/12/0 and ASI-INAF n. 2017-14-H.O. L.D. thanks Andrea Tramacere, Denys Malyshev, and Samuele Chimento for the useful advice that helped improve some aspects of this work.

## DATA AVAILABILITY

Data of specific test simulations can be obtained upon reasonable request from the corresponding author.

## REFERENCES

- Acciari V. A., et al., 2011, *ApJ*, 733, 96  
 Aharonian F. A., Atoyan A. M., 1996, *A&A*, 309, 917  
 Aharonian F. A., Atoyan A. M., 2000, *A&A*, 362, 937  
 Aharonian F. A., Plyasheshnikov A. V., 2003, *Astroparticle Physics*, 19, 525  
 Anchordoqui L. A., Torres D. F., McCauley T. P., Romero G. E., Aharonian F. A., 2003, *ApJ*, 589, 481  
 Arnason R. M., Papei H., Barmby P., Bahramian A., Gorski M. D., 2021, *MNRAS*, 502, 5455  
 Atwood W. B., et al., 2009, *ApJ*, 697, 1071  
 Bailer-Jones C. A. L., Rybizki J., Foesneau M., Demleitner M., Andrae R., 2021, *AJ*, 161, 147  
 Bednarek W., 1993, *A&A*, 278, 307  
 Bednarek W., 1997, *A&A*, 322, 523  
 Bednarek W., 2000, *A&A*, 362, 646  
 Bednarek W., 2009a, *MNRAS*, 397, 1420  
 Bednarek W., 2009b, *A&A*, 495, 919  
 Bellm E. C., et al., 2014, *ApJ*, 792, 108  
 Berestetskii V., Lifshitz E., Pitaevskii L., 1982, *Quantum Electrodynamics: Volume 4. Course of theoretical physics*, Pergamon Press  
 Berezinsky V., Kalashev O., 2016, *Phys. Rev. D*, 94, 023007  
 Bhadkamkar H., Ghosh P., 2012, *ApJ*, 746, 22  
 Bonnet-Bidaud J. M., Chardin G., 1988, *Phys. Rep.*, 170, 325  
 Camero-Arranz A., et al., 2012, *ApJ*, 754, 20  
 Campbell C. G., 1987, *MNRAS*, 229, 405  
 Cavallo G., Gould R. J., 1971, *Nuovo Cimento B Serie*, 2B, 77  
 Chadwick P. M., McComb T. J. L., Turver K. E., 1990, *Journal of Physics G: Nuclear and Particle Physics*, 16, 1773  
 Cheng K. S., Ruderman M., 1989, *ApJ*, 337, L77  
 Cheng K. S., Ruderman M., 1991, *ApJ*, 373, 187  
 Cheng K. S., Yu K. N., Cheung T., Lau M. M., 1991, *ApJ*, 379, 290  
 Cheng K. S., Lau M. M., Cheung T., Leung P. P., Ding K. Y., 1992, *ApJ*, 390, 480  
 Coe M. J., Reig P., McBride V. A., Galache J. L., Fabregat J., 2006, *MNRAS*, 368, 447  
 Coe M. J., et al., 2007, *MNRAS*, 378, 1427  
 Cooray A., 2016, *Royal Society Open Science*, 3, 150555  
 Daugherty J. K., Harding A. K., 1983, *ApJ*, 273, 761

- Davidson K., Ostriker J. P., 1973, *ApJ*, **179**, 585
- De Angelis A., Galanti G., Roncadelli M., 2013, *MNRAS*, **432**, 3245
- Di Salvo T., Sanna A., 2022, in Bhattacharyya S., Papitto A., Bhattacharya D., eds, *Astrophysics and Space Science Library Vol. 465*, Astrophysics and Space Science Library. pp 87–124, doi:10.1007/978-3-030-85198-9\_4
- Dubus G., 2006, *A&A*, **456**, 801
- Dubus G., 2013, *A&ARv*, **21**, 64
- El Mellah I., Sander A. A. C., Sundqvist J. O., Keppens R., 2019, *A&A*, **622**, A189
- Erber T., 1966, *Reviews of Modern Physics*, **38**, 626
- Finger M. H., Wilson R. B., Harmon B. A., 1996, *ApJ*, **459**, 288
- Fortin F., García F., Simaz Bunzel A., Chaty S., 2023, *A&A*, **671**, A149
- Frank J., King A., Raine D. J., 2002, *Accretion Power in Astrophysics: Third Edition*
- Gaissner T. K., 1990, *Cosmic rays and particle physics.* Cambridge and New York, Cambridge University Press
- García F., Aguilera D. N., Romero G. E., 2014, *A&A*, **565**, A122
- Ge M. Y., et al., 2020, *ApJ*, **899**, L19
- Ghosh P., 2007, *Rotation and Accretion Powered Pulsars.* World Scientific Series in Astronomy and Astrophysics Vol. 10, World Scientific Publishing Co., Pte. Ltd., Singapore, 2007, doi:10.1142/4806
- Ghosh P., Lamb F. K., 1979a, *ApJ*, **232**, 259
- Ghosh P., Lamb F. K., 1979b, *ApJ*, **234**, 296
- Gould R. J., Schröder G. P., 1967, *Physical Review*, **155**, 1404
- Grove J. E., Kurfess J. D., Philips B. F., Strickman M. S., Ulmer M. P., 1995, in *International Cosmic Ray Conference*. p. 1
- Harvey M., Rulten C., Chadwick P., 2022a, in *37th International Cosmic Ray Conference*. 12-23 July 2021. Berlin. p. 621 (arXiv:2107.07215)
- Harvey M., Rulten C. B., Chadwick P. M., 2022b, *MNRAS*, **512**, 1141
- Hayasaki K., Okazaki A. T., 2004, *MNRAS*, **350**, 971
- Heinz S., Sunyaev R., 2002, *A&A*, **390**, 751
- Hou X., Zhang W., Torres D. F., Ji L., Li J., 2023, *ApJ*, **944**, 57
- Huentemeyer P., BenZvi S., Dingus B., Fleischhack H., Schoorlemmer H., Weisgarber T., 2019, in *Bulletin of the American Astronomical Society*. p. 109 (arXiv:1907.07737), doi:10.48550/arXiv.1907.07737
- Jackson J. D., 1975, *Classical electrodynamics.* New York: Wiley, 1975, 2nd ed.
- Jafari A., Vishniac E. T., 2018, *ApJ*, **854**, 2
- Kanbach G., et al., 1989, *Space Sci. Rev.*, **49**, 69
- Katz J. I., Smith I. A., 1988, *ApJ*, **326**, 733
- Kendziorra E., et al., 1994, *A&A*, **291**, L31
- Kiraly P., Meszaros P., 1988, *ApJ*, **333**, 719
- Kluźniak W., Rappaport S., 2007, *ApJ*, **671**, 1990
- Levine A. M., Corbet R., 2006, *The Astronomer's Telegram*, **940**, 1
- Li J., Torres D. F., Zhang S., Papitto A., Chen Y., Wang J.-M., 2012, *ApJ*, **761**, 49
- Liu Q. Z., van Paradijs J., van den Heuvel E. P. J., 2006, *A&A*, **455**, 1165
- Lundy M., 2021, arXiv e-prints, p. arXiv:2108.09350
- Makishima K., Maejima Y., Mitsuda K., Bradt H. V., Remillard R. A., Tuohy I. R., Hoshi R., Nakagawa M., 1986, *ApJ*, **308**, 635
- Mirabel I. F., 2006, *Science*, **312**, 1759
- Motch C., Stella L., Janot-Pacheco E., Mouchet M., 1991, *ApJ*, **369**, 490
- Motz J. W., Olsen H. A., Koch H. W., 1969, *Reviews of Modern Physics*, **41**, 581
- Nagase F., et al., 1982, *ApJ*, **263**, 814
- Naso L., Kluźniak W., Miller J. C., 2013, *MNRAS*, **435**, 2633
- Neumann M., Avakyan A., Doroshenko V., Santangelo A., 2023, arXiv e-prints, p. arXiv:2303.16137
- Ochelkov I. P., Usov V. V., 1980, *Ap&SS*, **69**, 439
- Ong R. A., 1998, *Physics Reports*, **305**, 93
- Orellana M., Romero G. E., 2005, *Ap&SS*, **297**, 167
- Orellana M., Romero G. E., Pellizza L. J., Vidrih S., 2007, *A&A*, **465**, 703
- Papitto A., Torres D. F., Li J., 2014, *MNRAS*, **438**, 2105
- Paredes J. M., Bordas P., 2019, *Rendiconti Lincei. Scienze Fisiche e Naturali*, **30**, 107
- Penna R. F., Sądowski A., Kulkarni A. K., Narayan R., 2013, *MNRAS*, **428**, 2255
- Protheroe R. J., 1986, *MNRAS*, **221**, 769
- Protheroe R. J., Mastichiadis A., Dermer C. D., 1992, *Astroparticle Physics*, **1**, 113
- Rajoelimanana A. F., Charles P. A., Meintjes P. J., Townsend L. J., Schurch M. P. E., Udalski A., 2017, *MNRAS*, **464**, 4133
- Reig P., 2011, *Ap&SS*, **332**, 1
- Revnitsev M., Mereghetti S., 2015, *Space Sci. Rev.*, **191**, 293
- Riquelme M. S., Torrejón J. M., Negueruela I., 2012, *A&A*, **539**, A114
- Romano P., 2015, *Journal of High Energy Astrophysics*, **7**, 126
- Romanova M. M., Koldoba A. V., Ustyugova G. V., Blinova A. A., Lai D., Lovelace R. V. E., 2021, *MNRAS*, **506**, 372
- Romero G. E., Kaufman Bernadó M. M., Combi J. A., Torres D. F., 2001, *A&A*, **376**, 599
- Romero G. E., Okazaki A. T., Orellana M., Owocki S. P., 2007, *A&A*, **474**, 15
- Rosenberg F. D., Eyles C. J., Skinner G. K., Willmore A. P., 1975, *Nature*, **256**, 628
- Rossi B., Greisen K., 1941, *Rev. Mod. Phys.*, **13**, 240
- Rudak B., Meszaros P., 1991, *ApJ*, **383**, 269
- Rybicki G. B., Lightman A. P., 1979, *Radiative processes in astrophysics.* Wiley-Interscience Publication, New York: Wiley
- Scuderi S., et al., 2022, *Journal of High Energy Astrophysics*, **35**, 52
- Sguera V., 2009, arXiv e-prints, p. arXiv:0902.0245

- Sguera V., Romero G. E., Bazzano A., Masetti N., Bird A. J., Bassani L., 2009, *ApJ*, **697**, 1194
- Sguera V., Drave S. P., Bird A. J., Bazzano A., Landi R., Ubertini P., 2011, *MNRAS*, **417**, 573
- Shakura N. I., Sunyaev R. A., 1973, *A&A*, **500**, 33
- Shklovsky I. S., 1967, *ApJ*, **148**, L1
- Sidoli L., 2013, arXiv e-prints, p. [arXiv:1301.7574](https://arxiv.org/abs/1301.7574)
- Sierpowska A., Bednarek W., 2005, *MNRAS*, **356**, 711
- Smith I. A., Katz J. I., Diamond P. H., 1992, *ApJ*, **388**, 148
- Stecker F. W., 1971, Cosmic gamma rays. Vol. 249, NTRS - NASA Technical Reports Server
- Stollberg M. T., Finger M. H., Wilson R. B., Harmon B. A., Rubin B. C., Zhang N. S., Fishman G. J., 1993, *IAU Circ.*, **5836**, 1
- Tavani M., et al., 2009, *A&A*, **502**, 995
- Torres D. F., Pessah M. E., Romero G. E., 2001, *Astronomische Nachrichten*, **322**, 223
- Treves A., Maraschi L., Abramowicz M., 1988, *PASP*, **100**, 427
- Vercellone S., et al., 2022, *Journal of High Energy Astrophysics*, **35**, 1
- Vietri M., 2008, Foundations of high-energy astrophysics. Theoretical astrophysics, Chicago : University of Chicago Press, 2008., <http://pi.lib.uchicago.edu/1001/cat/bib/11187539>
- Walter R., 2007, *Ap&SS*, **309**, 5
- Wang Y. M., 1995, *ApJ*, **449**, L153
- Wang Y. M., 1996, *ApJ*, **465**, L111
- Wang W., et al., 2021, *Journal of High Energy Astrophysics*, **30**, 1
- Weekes T. C., 1988, *Physics Reports*, **160**, 1
- White N. E., Nagase F., Parmar A. N., 1995, in X-ray Binaries. pp 1–57
- Wilson R. B., et al., 1994, in Holt S., Day C. S., eds, American Institute of Physics Conference Series Vol. 308, The Evolution of X-ray Binaries. p. 451, [doi:10.1063/1.45985](https://doi.org/10.1063/1.45985)
- Xing Y., Wang Z., 2019, *ApJ*, **882**, 112
- Zhang J.-F., Jin H., Dong A.-J., 2014a, *Research in Astronomy and Astrophysics*, **14**, 285
- Zhang S. N., et al., 2014b, in Takahashi T., den Herder J.-W. A., Bautz M., eds, Society of Photo-Optical Instrumentation Engineers (SPIE) Conference Series Vol. 9144, Space Telescopes and Instrumentation 2014: Ultraviolet to Gamma Ray. p. 91440X ([arXiv:1407.4866](https://arxiv.org/abs/1407.4866)), [doi:10.1117/12.2055280](https://doi.org/10.1117/12.2055280)
- van Paradijs J., 1998, in Bucccheri R., van Paradijs J., Alpar A., eds, NATO Advanced Study Institute (ASI) Series C Vol. 515, The Many Faces of Neutron Stars.. p. 279 ([arXiv:astro-ph/9802177](https://arxiv.org/abs/astro-ph/9802177))

## APPENDIX A: GENERAL OUTLINE OF THE PROCEDURE TO CALCULATE THE OBSERVABLE $\gamma$ -RAY EMISSION

Figure A1 shows a flow-chart to describe the main aspects of the procedure used to calculate the  $\gamma$ -ray emission from an XRB. It can be divided in five steps:

- (i) input parameters;
- (ii) calculation of the proton energies and production of  $\gamma$ -ray primary photons inside the accretion disc;
- (iii) calculation of the cascades produced inside of the accretion disc;
- (iv) calculation of the cascades produced outside the accretion disc;
- (v) Output of the list of photons arriving at the observer, the expected observed flux and spectrum above 10 GeV.

Other details are given in Sect. 2.4.

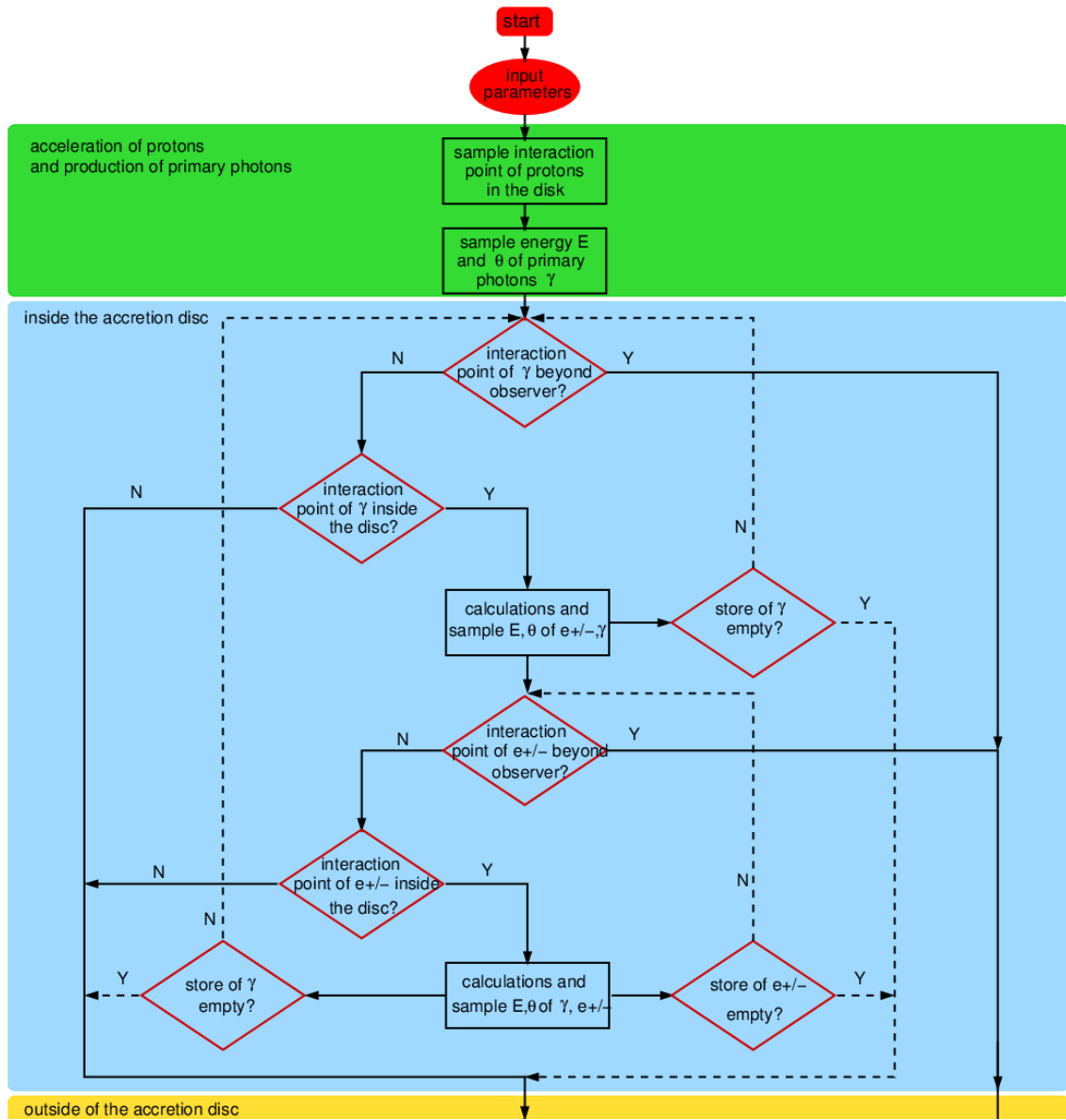


**Figure A1.** Schematic representation illustrating the computational procedure for calculating the expected observable  $\gamma$  – ray emission (for the second part of the flow-chart, see next figure). Some lines are dotted for ease of understanding when they cross other lines.

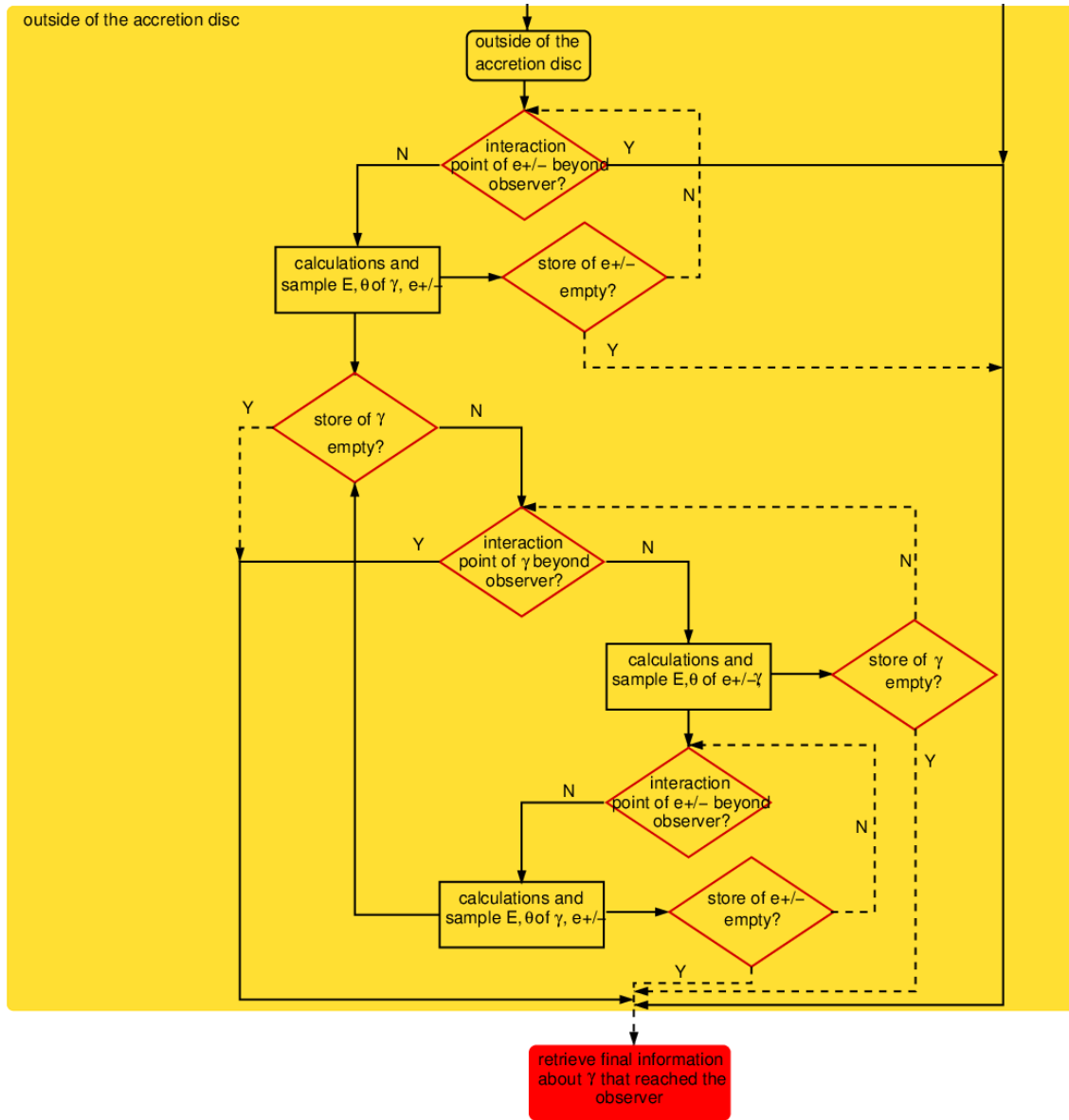


**Figure A1** – *continued* Second part of the schematic representation illustrating the computational procedure for calculating the expected observable  $\gamma$ -ray emission.

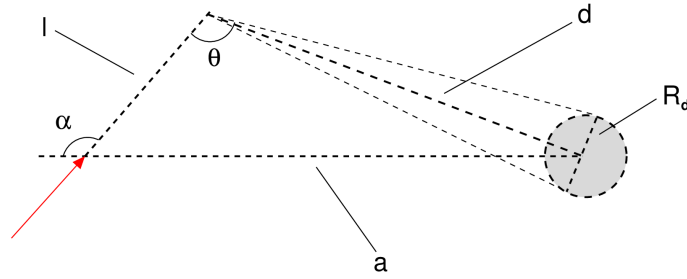


**Figure B1.** Schematic view of a binary system composed by a NS, where a  $\gamma$ -ray photon (red arrow) is injected with an angle  $\alpha$ , and a donor star with radius  $R_d$ . The stars are separated by a distance  $a$ .

## APPENDIX B: OPTICAL DEPTH FOR $\gamma$ -RAY PHOTONS IN THE PHOTON FIELD OF A MASSIVE STAR

Following an approach similar to that described in [Bednarek \(1997\)](#), we assume that a  $\gamma$ -ray photon with energy  $E_\gamma$  is injected with an angle  $\alpha$  at a distance  $a$  from the center of the companion star (Fig. B1). Following [Gould & Schröder \(1967\)](#) (their eq. 7), the optical depth for the propagation of the  $\gamma$ -ray photon in the radiation field of the donor star is given by:

$$\tau = \int_{R_0}^D \int_{\theta_{\min}}^{\theta_{\max}} \int_{\varepsilon(s>1)}^{\infty} \frac{1}{2} \sigma_{\gamma\gamma}(\beta) n(\varepsilon, d(l)) (1 - \cos \theta) \sin \theta \varepsilon d \varepsilon d \theta dl, \quad (\text{B1})$$

where  $D$  is the distance from the observer,  $R_0$  is the inner radius of the accretion disc around the NS,  $\theta$  is the angle of interaction between the  $\gamma$ -ray photon and the soft photons,  $n(\varepsilon, d)$  is the blackbody photon number density at a distance  $d$  from the donor star,  $\sigma_{\gamma\gamma}(\beta)$  is the cross section for  $e^\pm$  pair production in two photon collision ([Gould & Schröder 1967](#), and references therein).  $\beta$  is given by:

$$\beta = \sqrt{1 - \frac{1}{s}}$$

$$s = \frac{\varepsilon E_\gamma}{2m_e^2 c^4} (1 - \cos \theta),$$

Obviously, for pair production to occur,  $s > 1$ . The angle of interaction  $\theta$  varies from  $\theta_{\min}$  and  $\theta_{\max}$ , due to the size of the donor star. These angles are given by:

$$\theta = \arctan\left(\frac{a - l \cos(\pi - \alpha)}{l \sin(\pi - \alpha)}\right) + \alpha - \frac{\pi}{2}$$

$$\theta_{\min} = \theta - \arctan\left(\frac{R_d}{d}\right)$$

$$\theta_{\max} = \theta + \arctan\left(\frac{R_d}{d}\right)$$

Equation (B1) provides only a rough estimate of the optical depth. For example, we neglected the spherical shape of the donor star, being, for the cases of our interest,  $a \gg R_d$ . A detailed study (whose solutions are valid for binary systems with narrower orbits than those considered in this work) can be found in [Bednarek \(1997\)](#).

## APPENDIX C: CONTRIBUTION OF DIFFERENT INTERACTION PROCESSES TO THE $\gamma$ -RAY SPECTRUM: WEAK SHIELDING CASE

Table C1 and Fig. C1 show the observable  $\gamma$ -ray luminosities and spectra (above 10 GeV) calculated assuming a weakly shielded gap, four different X-ray luminosities, and different types of interactions processes activated. In particular, Fig. C1 shows the  $\gamma$ -ray spectra (above 10 GeV) from photons that escaped from the accretion disc, those observed (i.e. photons that escaped from the disc and survived along their journey between the source and the observer), and the spectrum of the primary photons (those created by the  $\pi^0$  decay inside the disc). Figure C2 shows, for each of the simulations displayed in Fig. C1, how the cascade of  $\gamma$ -ray photons develops inside and outside the disc. Similar results for the strong shielding case are described in Sect. 3.1.

This paper has been typeset from a  $\text{\TeX}/\text{\LaTeX}$  file prepared by the author.



**Table C1.**  $\gamma$ -ray luminosities ( $\geq 10$  GeV), for the primary photons ( $L_{\text{pri}}$ ), photons which escaped from the disc ( $L_{\text{esc}}$ ), and photons which reached the observer ( $L_{\text{obs}}$ ), assuming weak shielding, for different X-ray luminosities, and for different radiation and pair processes activated. We assumed  $B = 4 \times 10^{12}$  G (i.e. a framework compatible with the Be/XRB A0535+26).

$L_x$	$L_\gamma$	Case A <sup>a</sup>	Case B <sup>b</sup>	Case C <sup>c</sup>
		nuclei	nuclei + photons	nuclei + photons + $\vec{B}$
		erg s <sup>-1</sup>	erg s <sup>-1</sup>	erg s <sup>-1</sup>
$3 \times 10^{36}$	$L_{\text{pri}}$	$1.37 \pm 0.20 \times 10^{31}$	$1.36 \pm 0.14 \times 10^{31}$	$1.21 \pm 0.16 \times 10^{31}$
	$L_{\text{esc}}$	$8.08 \pm 2.62 \times 10^{30}$	$7.52 \pm 1.80 \times 10^{30}$	$7.45 \pm 1.78 \times 10^{30}$
	$L_{\text{obs}}$	$8.08 \pm 2.62 \times 10^{30}$	$6.35 \pm 1.65 \times 10^{30}$	$6.43 \pm 1.66 \times 10^{30}$
$5 \times 10^{36}$	$L_{\text{pri}}$	$6.44 \pm 0.64 \times 10^{31}$	$6.51 \pm 0.64 \times 10^{31}$	$6.68 \pm 0.62 \times 10^{31}$
	$L_{\text{esc}}$	$2.62 \pm 0.46 \times 10^{31}$	$2.71 \pm 0.46 \times 10^{31}$	$2.57 \pm 0.45 \times 10^{31}$
	$L_{\text{obs}}$	$2.62 \pm 0.46 \times 10^{31}$	$9.07 \pm 2.61 \times 10^{30}$	$7.96 \pm 2.44 \times 10^{30}$
$7 \times 10^{36}$	$L_{\text{pri}}$	$1.25 \pm 0.13 \times 10^{32}$	$1.26 \pm 0.14 \times 10^{32}$	$1.27 \pm 0.13 \times 10^{32}$
	$L_{\text{esc}}$	$4.54 \pm 0.72 \times 10^{31}$	$4.19 \pm 0.69 \times 10^{31}$	$3.19 \pm 0.61 \times 10^{31}$
	$L_{\text{obs}}$	$4.54 \pm 0.72 \times 10^{31}$	$3.00 \pm 1.25 \times 10^{30}$	$1.88 \pm 1.03 \times 10^{30}$
$10^{37}$	$L_{\text{pri}}$	$2.39 \pm 0.26 \times 10^{32}$	$2.36 \pm 0.44 \times 10^{32}$	$2.36 \pm 0.44 \times 10^{32}$
	$L_{\text{esc}}$	$5.67 \pm 0.98 \times 10^{31}$	$5.26 \pm 0.26 \times 10^{31}$	$3.22 \pm 0.15 \times 10^{31}$
	$L_{\text{obs}}$	$5.67 \pm 0.98 \times 10^{31}$	$6.43 \pm 1.00 \times 10^{29}$	$1.89 \pm 0.63 \times 10^{29}$

<sup>a</sup> Case A: interaction with nuclei: pair production in the Coulomb field of nucleus and bremsstrahlung.

<sup>b</sup> Case B: interaction with nuclei and photons from the accretion disc: pair production in the Coulomb field of nucleus, pair production in photon-photon collisions, bremsstrahlung, inverse Compton with soft photons from the accretion disc.

<sup>c</sup> Case C: interaction with nuclei and photons from the accretion disc, and with the magnetic field: pair production in the Coulomb field of nucleus, pair production in photon-photon collisions, magnetic pair production, bremsstrahlung, inverse Compton with soft photons from the accretion disc, synchrotron, and curvature.

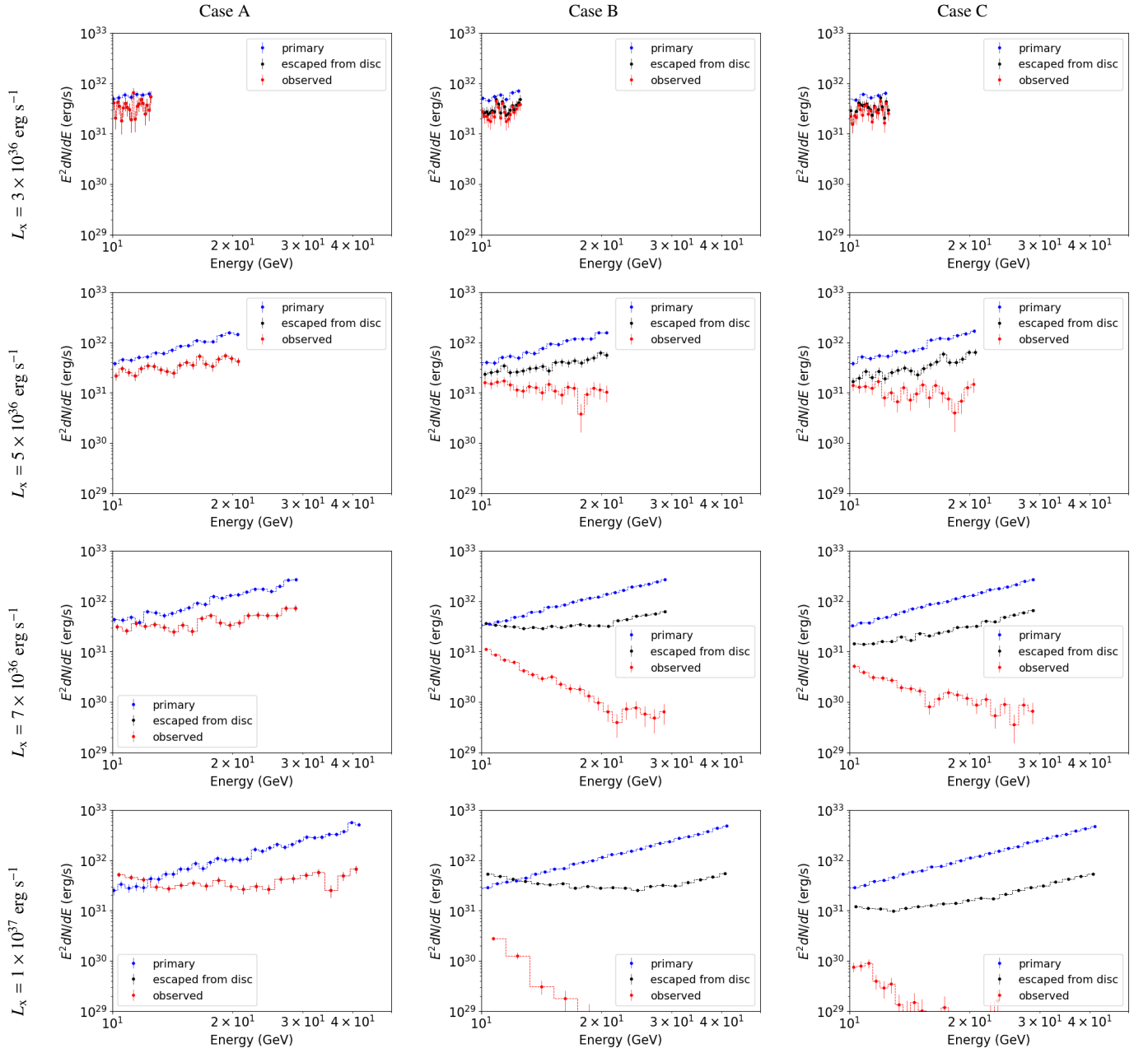


**Figure C1.**  $\gamma$ -ray spectra for the primary photons, photons which escaped from the disc, and photons which reached the observer, for different X-ray luminosities, and for different radiation and pair processes activated, as described in Table C1. We assumed  $B = 4 \times 10^{12}$  G (i.e. a framework compatible with the Be/XRB A0535+26) and a weak shielded gap.

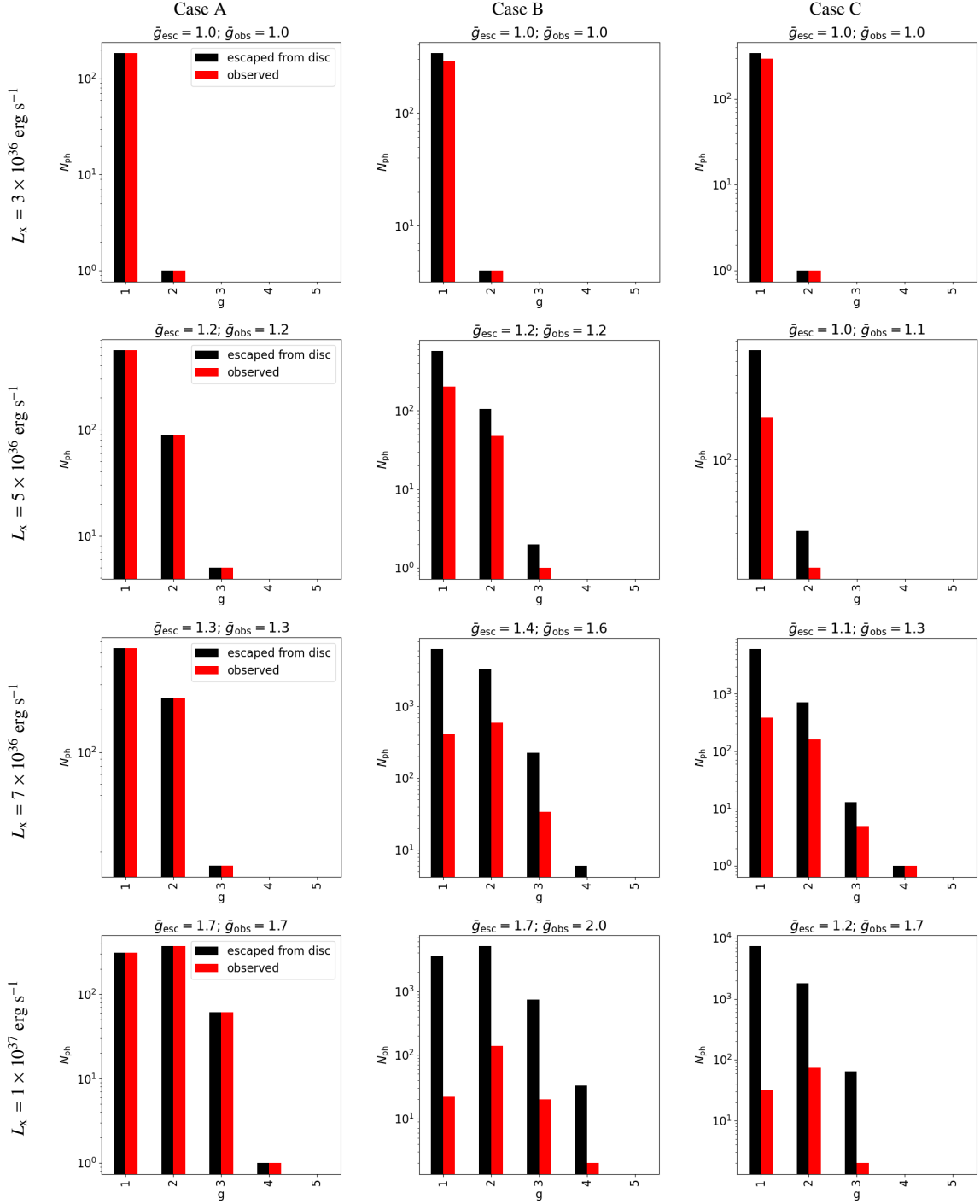


**Figure C2.** Histograms of the generations of photons that escape from the disc (black histogram) and reach the observer (red histogram), for different X-ray luminosities and radiation and pair processes activated as described in Table 2. We assumed  $B = 4 \times 10^{12}$  G (i.e. a framework compatible with the Be/XRB A0535+26) and a weak shielded gap. On top of each panel is shown the average value of the generation number for photons that escaped the disc ( $\bar{g}_{\text{esc}}$ ) and those that reached the observer ( $\bar{g}_{\text{obs}}$ ).